14 Jun 2022

Preparation of Carbon Aerogels from Polymer-Cross-Linked Xerogel Powders Without Supercritical Fluid Drying and their Application in Highly Selective CO2Adsorption

Rushi U. Soni

Vaibhav A. Edlabadkar

Daniel Greenan

Parwani M. Rewatkar

et. al. For a complete list of authors, see https://scholarsmine.mst.edu/chem_facwork/3189

Recommended Citation

R. U. Soni et al., "Preparation of Carbon Aerogels from Polymer-Cross-Linked Xerogel Powders Without Supercritical Fluid Drying and their Application in Highly Selective CO2Adsorption," *Chemistry of Materials*, vol. 34, no. 11, pp. 4828 - 4847, American Chemical Society, Jun 2022.
The definitive version is available at https://doi.org/10.1021/acs.chemmater.1c04170

CHEMISTRY OF MATERIALS

pubs.acs.org/cm

Article

Preparation of Carbon Aerogels from Polymer-Cross-Linked Xerogel Powders without Supercritical Fluid Drying and Their Application in Highly Selective CO_2 Adsorption

Rushi U. Soni, Vaibhav A. Edlabadkar, Daniel Greenan, Parwani M. Rewatkar, Nicholas Leventis, and Chariklia Sotiriou-Leventis*

Cite This: *Chem. Mater.* 2022, 34, 4828−4847

Read Online

ACCESS | Metrics & More | Article Recommendations | Supporting Information

ABSTRACT: Carbon aerogels are well-known materials for their high porosity and high surface areas. They are typically made from pyrolysis of carbonizable polymeric aerogels. Here, we report an alternative route to monolithic carbon aerogels starting from xerogel powders. Use of powders speeds up solvent exchanges along sol−gel processing, and xerogelling bypasses the supercritical fluid drying step that is needed for making polymeric aerogels. Overall, this alternative route results in time, energy, and materials efficiency in the fabrication of carbon aerogels. Specifically, polymer-cross-linked silica xerogel powders were prepared via free-radical surface-initiated polymerization of acrylonitrile (AN) on a suspension of silica particles derived from tetramethylorthosilicate (TMOS) surface modified with 3-aminopropyltriethoxysilane (APTES)-derived initiator. Alternatively, cross-linked silica xerogel powders were prepared with a carbonizable polyurea (PUA) derived from the reaction of an aromatic triisocyanate (tris(4-isocyanatophenyl)methane) with −OH, $-NH_2$, and adsorbed water on the surface of a TMOS/APTES-derived silica suspension. Wet-gel powders by either method were dried under vacuum at 50 °C to xerogel powders, which were compressed into discs. In turn, these discs were carbonized and then they were treated with HF to remove silica and with CO_2 to create microporosity. The resulting monolithic carbon aerogels had porosities up to 83% v/v, Brunauer−Emmett−Teller (BET) surface areas up to 1934 $m^2\ g^{-1}$, and could uptake up to 9.15 mmol g^{-1} of CO_2 at 273 K, with high selectivity over H_2, N_2, and CH_4.

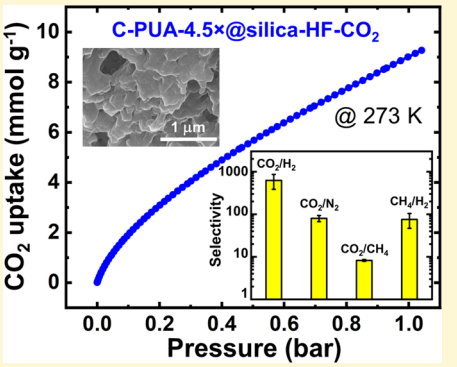

1. INTRODUCTION

Carbon aerogels are electrically conducting low-density materials with high internal surface area. They typically consist of over 90% w/w of carbon. They are made with pyrolysis of carbonizable polymeric aerogels, which in turn are prepared with typical sol−gel chemistry. Applications of carbon aerogels include gas adsorption,[1] gas separation,[2] water purification,[3] use as catalyst supports,[4] and electrodes for fuel cells.[5] Polymeric precursors of carbon aerogels include aromatic polyureas, polyacrylonitrile, polyamides, polyimides, and most commonly phenolic resins (e.g., those from resorcinol−formaldehyde) including polybenzoxazines.[6−9] The high porosity and surface area of carbon aerogels come from both the innate porosity of the parent polymeric aerogels and to a lesser extent from the chemical transformations (decomposition) of the skeletal framework during pyrolysis.

Aerogel-like porous carbon materials have also been based on three-dimensional (3D) assemblies of carbon nanotubes,[10,11] carbon nanofibers,[12] templated porous carbons, and graphene-based materials.[13] In the end, the porosity and surface area of all aerogel and aerogel-like porous carbons can be enhanced using one or more of the so-called activation (etching) processes either at low temperatures with reagents such as KOH, NaOH, $ZnCl_2$, $FeCl_2$,[14−17] or at high temperatures, typically in tandem with the carbonization process, using steam, air, or CO_2.[18]

Both the synthesis of polymeric aerogel precursors of carbon aerogels and the direct 3D assembly of carbonaceous materials into aerogel-like structures involve drying of wet gels first by extracting the pore-filling solvent with liquid CO_2 and subsequently by converting liquid CO_2 to a supercritical fluid (SCF) that is vented off as a gas. This time-tested method eliminates the surface tension forces of an evaporating solvent through the delicate skeletal framework of the wet gel and thus preserves its volume and structure in the final dry object (the aerogel). On the downside, use of supercritical fluids is a high-pressure, energy-intensive process. When it comes to the preparation of monolithic carbon aerogels with a predeter-

Received: December 6, 2021
Revised: April 11, 2022
Published: May 16, 2022

https://doi.org/10.1021/acs.chemmater.1c04170
Chem. Mater. 2022, 34, 4828−4847

Scheme 1. Monomers and Surface Modifiers for Latching Carbonizable Polymers to Silica

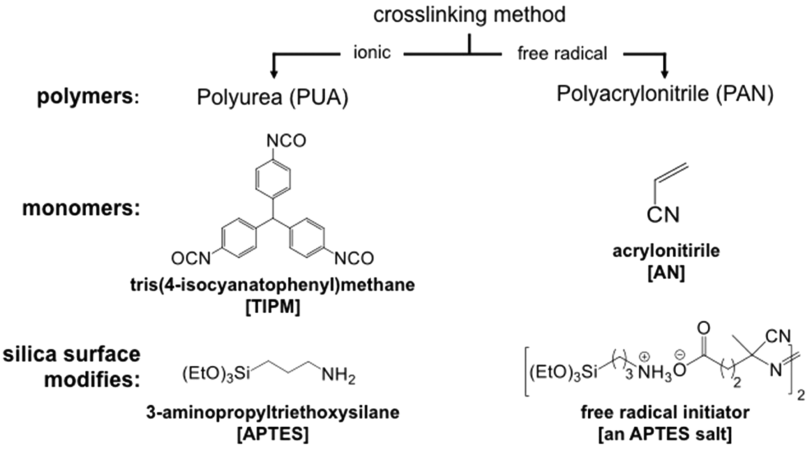

mined form factor, molding and handling of potentially fragile polymeric wet-gel and aerogel precursors more often than not lower the yield of the monoliths with the intended shape. Furthermore, the size of the monoliths is limited by the size of the pressure vessel. Conversely, if the pore-filling solvent of a wet gel is allowed to evaporate under ambient pressure, surface-tension-induced shrinkage is extensive and results in higher-density, low-porosity solids referred to as xerogels.[19] Xerogels can be obtained in the form of powders by drying suspensions of wet-gel microparticles, which in turn are obtained by applying vigorous stirring of the sol during gelation that disrupts long-range gel formation. Wet-gel microparticles are easy to handle and can be dried quickly due to their high surface-to-volume ratios.[20]

Along these lines, a new hybrid approach to aerogels-via-xerogels was demonstrated recently with the preparation of ceramic (silicon carbide and silicon nitride)[20] and metallic (cobalt)[21] aerogels via pyrolysis of compressed xerogel-powder compacts. The xerogel powders consisted of a typical sol−gel-derived nanostructured oxide network coated conformally (cross-linked) with an about stoichiometrically balanced carbonizable polymer. Carbothermal reduction of the oxide network produced the ceramic or metallic network and created porosity by consuming all carbon in the composite. The sol−gel-derived oxide network in use was silica in the cases of SiC and Si_3N_4 aerogels and cobaltia in the case of Co(0) aerogels. In the case of the ceramic aerogels, the pyrolysis temperature was about 1500 °C and much lower (800 °C) in the case of cobalt aerogels. A small amount of unreacted carbon remaining at the end was removed oxidatively, creating more porosity. The method does not involve SCFs and is capable of furnishing monoliths in various shapes and sizes.

In this paper, we demonstrate the complimentary use of the aerogel-via-xerogel method in the synthesis of carbon aerogels. For this, the oxide partner in the cross-linked xerogel was silica; the mol ratio of the carbonizable polymer/silica was tilted heavily toward the polymeric component; the pyrolysis temperature stayed low (800 °C) to avoid the formation of SiC or Si_3N_4; and silica was removed at the end with hydrofluoric acid (HF). Overall, the porosity of the carbon aerogels by the aerogel-via-xerogel method was created by (a) the decomposition of the carbonizable polymer to carbon. and (b) the reactive removal of the silica network. Additional porosity was created using reactive etching (with CO_2 at 1000 °C/Ar) of the resulting carbon aerogels. The general material properties were similar to those of other carbon aerogels obtained via the traditional method, namely, via direct pyrolysis of polymeric aerogels from the SCF drying route. Typical porosities were over 80% v/v, and Brunauer−Emmett−Teller (BET) surface areas reached 1930 $m^2\ g^{-1}$. In terms of applications, these new types of carbon aerogels were tested for their adsorption capacity toward CO_2, and the values obtained and reported here were above the average of other CO_2 adsorbers.

2. RESULTS AND DISCUSSION

2.1. Materials Synthesis. The synthesis of carbon aerogels by the aerogel-via-xerogel method was carried out with two different carbonizable polymers: an aromatic polyurea (PUA) and polyacrylonitrile (PAN) (Scheme 1). Acting as a template for the growth of the carbonizable polymer, the silica network was obtained by gelation of tetramethylorthosilicate (TMOS) followed by modification with either 3-aminopropyltriethoxysilane (APTES) or with a free-radical initiator, which again was a derivative of APTES (Scheme 1). The specific polyurea as well as PAN was selected to test the applicability of the two major aerogel-cross-linking chemistries from the literature, namely, with isocyanates or with surface-initiated free-radical polymerization,[22] to the aerogels-via-xerogels concept.

As shown in Scheme 2A, both routes to carbons from polymer-cross-linked silica xerogel powders started with the preparation of sol−gel silica particle suspensions by mixing solution A (TMOS in methanol) with solution B (NH_4OH + water in methanol),[23] followed by adding the combined mixture in hexane under vigorous mechanical stirring.[20] As hydrolysis and condensation of TMOS progressed, the suspended silica particles turned the continuous phase (hexane) into milky white (~20 min).

2.1.1. Modification of Silica with Polyurea: PUA@silica Xerogel Powders. Referring to Scheme 2B, APTES was added to the suspension of the silica particles in a 4:1 TMOS/APTES mol/mol ratio. As shown previously, all postgelation added APTES is attached to the surface of silica down to the primary particle level; in fact, the resulting composition, referred to as APTES@silica, is identical to what is obtained when APTES is premixed with TMOS[20] and that has been considered as proof that hydrolysis and condensation of TMOS is faster than that of APTES.[24,25] The APTES@silica hexane suspension was aged at room temperature under vigorous stirring for 24 h. Conformal coating of the APTES@silica particles with

https://doi.org/10.1021/acs.chemmater.1c04170
Chem. Mater. 2022, 34, 4828−4847

Scheme 2. Synthesis of Silica Microparticle Suspensions, Cross-Linking with Carbonizable Polymers, Xerogel Powders, and Xerogel-Powder Compacts

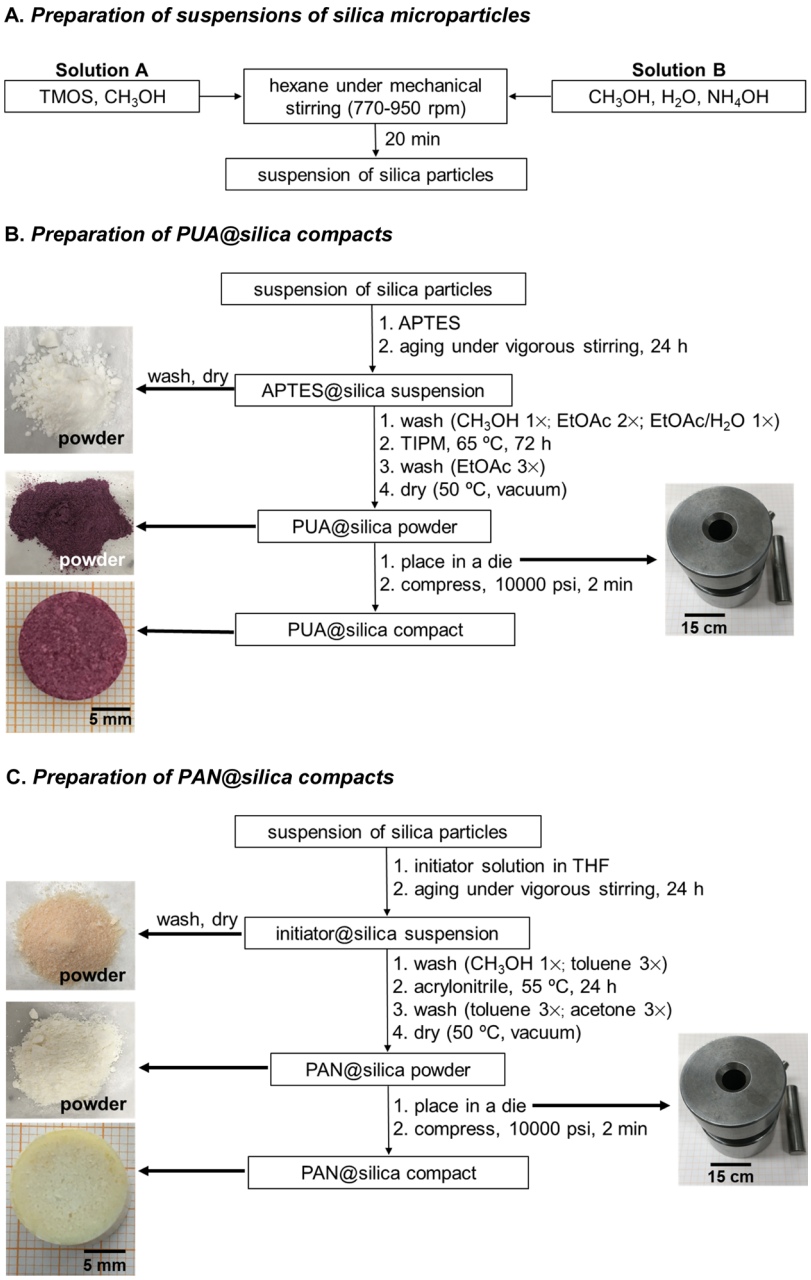

polyurea entails the reaction of a multifunctional isocyanate with both the $-NH_2$ groups from the APTES moiety and gelation water remaining adsorbed on the surface of silica.[22,26,27] To prepare a reproducible surface for this purpose, excess solvents were removed from the APTES@silica suspension using centrifugation, and the resulting rather thick paste was washed first with ethyl acetate and then with water-saturated ethyl acetate. For characterization purposes, a small part of the paste from the last centrifugation was separated and dried under vacuum at 50 °C. The remaining paste was cross-linked with three different concentrations of Desmodur RE, a commercially available ethyl acetate solution of TIPM—see Scheme 1, using 1.5×, 3×, or 4.5× mol/mol excess of TIPM relative to the total amount of silicon in APTES@silica. The resulting polyurea cross-linked wet-silica suspension was washed with ethyl acetate and was dried under vacuum at 50 °C to a free-flowing fine xerogel powder that is referred to as PUA-1.5×@silica(4:1), PUA-3×@silica(4:1), or PUA-4.5×@silica(4:1). The first numeral in the sample names designates the TIPM/silica mol/mol ratio in the cross-linking bath; the ratio in parentheses designates the TMOS/APTES mol/mol ratio in silica. Since that ratio does not change among samples, the sample names of the three different formulations with TIPM-derived polyurea are abbreviated as PUA-1.5×@silica, PUA-3×@silica, and PUA-4.5×@silica, and for simplicity, all three samples are referred to together as PUA@silica (Scheme 2B).

Using thermogravimetric analysis under O_2 (TGA, see Figure S.1A of Appendix I in the Supporting Information), at the high-temperature plateau (>600 °C), the APTES@silica powder had lost 18.8% of its mass, which was attributed to its organic component coming from APTES. The balance (81.2%

https://doi.org/10.1021/acs.chemmater.1c04170
Chem. Mater. 2022, 34, 4828−4847

Table 1. Composition of PUA@silica and of Carbonized C-PUA@silica Xerogel Compacts Prepared with Different TIPM/Silicon mol Ratios (1.5×, 3×, 4.5×)

	1.5×		3×		4.5×	
sample	PUA or C [% w/w]	SiO_2 [% w/w]	PUA or C [% w/w]	SiO_2 [% w/w]	PUA or C [% w/w]	SiO_2 [% w/w]
PUA@silica	74.1	21.0	77.7	18.1	84.1	12.9
C-PUA@silica (expected)[a]	66.4	33.6	70.6	29.4	78.5	21.5
C-PUA@silica (found)	64.0	36.0	70.1	29.9	75.5	24.5

[a]Calculated based on the composition of PUA@silica and the carbonization yield of TIPM-derived polyurea (56%).[28]

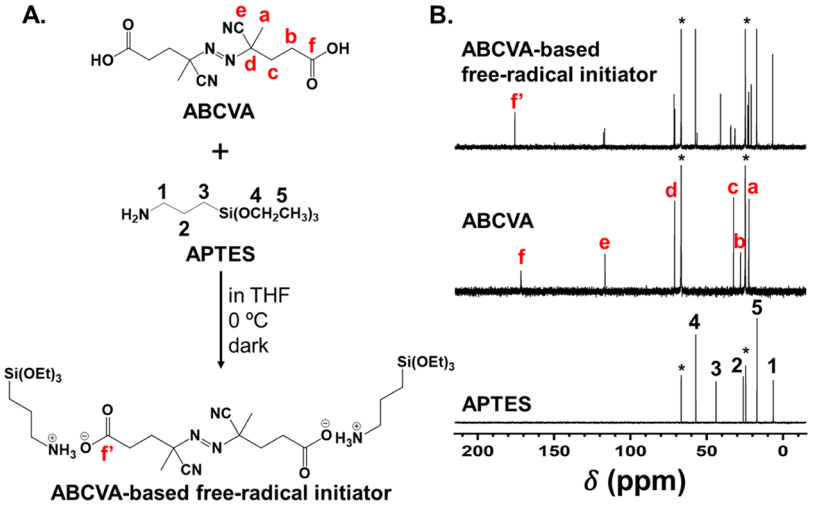

Figure 1. (A) Preparation of the bidentate free-radical initiator used in this study via an acid−base reaction of 4,4′-azobis-4-cyanovaleric acid (ABCVA) and APTES. (B) Liquid ^{13}C NMR spectra in THF-d_8 of APTES, ABCVA, and 3-triethoxysilylpropan-1-aminium 4,4′-azobis(4-cyanovalerate) (ABCVA-based free-radical initiator). (Solvent peaks are marked with asterisks).

w/w) was attributed to SiO_2. Under the same conditions, PUA-1.5×@silica, PUA-3×@silica, and PUA-4.5×@silica lost 79.0, 81.9, and 87.1% of their masses, respectively, attributed to the sum of the organic component coming from both APTES and the TIPM-derived polyurea. It was then calculated that PUA-2×@silica consisted of 21.0% w/w SiO_2 and 74.1% w/w of TIPM-derived polyurea, and so on as summarized in Table 1. Overall, the amount of polyurea increased from 74.1 to 84.1% as the TIPM/silicon mol/mol ratio increased from 1.5 to 4.5.

2.1.2. Modification of Silica with Polyacrylonitrile: PAN@silica Xerogel Powders. As outlined in Scheme 2C, polyacrylonitrile was coated conformally on the surface of sol−gel-derived silica particles via surface-initiated free-radical polymerization of acrylonitrile (AN). As shown in Figure 1A, the surface-confined initiator was the product of the room-temperature, acid−base reaction in anhydrous THF of 4,4′-azobis(4-cyanovaleric acid) (ABCVA), a −COOH group modified derivative of azobisisobutyronitrile (AIBN), and APTES, in an APTES/ABCVA mol/mol ratio of 2:1. In turn, Figure 1B compares the liquid ^{13}C NMR of the APTES/ABCVA reaction mixture with the spectra of the two components. Complete neutralization was confirmed by the conversion of the −COOH group to the carboxylate reflected in the downfield shift of the carboxylic carbon of ABCVA (f: 171 ppm) to 176 ppm (f′: carboxylate). As a bidentate species, the ABCVA-APTES salt is expected to attach itself to silica from both of its ends; therefore, the polymer produced by homolysis of the central −N═N− group would remain surface-bound. This concept is not new;[29,30] however, its implementation is the following: attachment of ABCVA on the surface of silica as a ABCVA-APTES salt comprises a significant simplification over the previous initiator design that involved linking covalently the −COOH functionality of ABCVA and the $-NH_2$ functionality of APTES as an amide.[29,30] It was reasoned that the simple $-NH_3^+$ $^-$OOC− salt will remain surface bound (a) because APTES is surface-bound covalently and (b) as long as the ionic strength of the solution filling the pores of the wet gel is zero.

The as-prepared initiator solution was added to a silica suspension, which in turn had been prepared as shown in Scheme 2A. The amount of the initiator solution was adjusted so that the final TMOS/APTES ratio would be equal to either 9:1 or 7:3 mol/mol. Those ratios were chosen to bracket in the middle the TMOS/APTES ratio (4:1) that was used in the preparation of PUA@silica and thus use the PAN series of materials to probe not only the effect of the cross-linking polymer but also the effect, if any, of the polymer anchoring chemistry and the aptitude of the surface to uptake polymer on the material properties of the final carbons. Thus, the resulting suspension was aged for 24 h under vigorous stirring, while the apparatus was covered with Al foil. The resulting wet-silica suspension was referred to as initiator@silica. The gelation solvents were removed with centrifugation, and the resulting wet initiator@silica paste was washed with methanol (1×) and then with toluene (3×). For characterization purposes, some of the initiator@silica paste was collected right before the first toluene wash and was dried under vacuum at 23 °C in the dark. Toluene-washed initiator@silica paste was cross-linked with PAN in an acrylonitrile (AN)−toluene solution at 55 °C for 24 h using two different inhibitor-free AN-to-silicon ratios (AN/silicon = 2 and 6 mol/mol). The resulting PAN-cross-

https://doi.org/10.1021/acs.chemmater.1c04170
Chem. Mater. 2022, 34, 4828−4847

Table 2. Composition of PAN@Silica and of Carbonized C-PAN@Silica Xerogel Compacts Prepared with Different Acrylonitrile/SiO_2 ($n\times$) and TMOS/APTES (x:y) mol Ratios

	6×, (9:1)		2×, (9:1)		6×, (7:3)		2×, (7:3)	
sample	PAN or C [% w/w]	SiO_2 [% w/w]	PAN or C [% w/w]	SiO_2 [% w/w]	PAN or C [% w/w]	SiO_2 [% w/w]	PAN or C [% w/w]	SiO_2 [% w/w]
PAN@silica	80.8	14.9	53.7	36.0	67.9	16.0	39.7	30.1
C-PAN@silica (expected)[a]	79.1	20.9	51.1	48.9	73.8	26.2	48.0	52.0
C-PAN@silica (found)	75.6	24.4	46.5	53.5	78.4	21.6	49.3	50.7

[a]Calculated based on the composition of PAN@silica and the carbonization yield of PAN (70%).[31,32]

linked wet-silica suspensions were washed with toluene and then with acetone and were dried under vacuum at 50 °C to free-flowing fine xerogel powders that are referred to as PAN-$n\times$@silica(x:y), where "$n\times$" stands for the molar excess of AN over total silicon in the cross-linking bath and, as just described, $n\times$ takes the values of 2× and 6×; x:y stands for the TMOS/APTES mol/mol ratio in the formulation of the silica backbone, and as it was described above, it takes the values of 9:1 and 7:3.

Using thermogravimetric analysis under O_2 (TGA, see Figure S.1B of Appendix I in the Supporting Information), at the high-temperature plateau (>600 °C), the initiator@silica powder had lost 22.3% of its mass, attributed to its organic component coming from the initiator. The balance (77.7% w/w) was attributed to SiO_2. Under the same conditions, PAN-6×@silica(9:1), PAN-2×@silica(9:1), PAN-6×@silica(7:3), and PAN-2×@silica(7:3) lost 85.1, 64.0, 84.0, and 69.9% of their masses, respectively, attributed to the sum of the organic component coming from both the initiator and PAN. It was then calculated that, for example, PAN-6×@silica(9:1) consisted of 14.9% w/w SiO_2 and 80.8% w/w of polyacrylonitrile, and so on as summarized in Table 2. Overall, for a given silica:initiator ratio (reminder: expressed as 9:1 or 7:3 in the sample names), the amount of PAN in PAN@silica increased as the monomer amount in the cross-linking bath increased. Interestingly, higher amounts of PAN had been uptaken in the PAN@silica composites with lower amounts of initiator, i.e., the percent amounts of PAN in the composites were higher when x:y = 9:1 than when x:y = 7:3.

2.1.3. Processing of PUA@Silica and PAN@Silica Compacts into Carbon Aerogels. Dry PUA@silica and PAN@silica powders were placed in suitable stainless-steel dies and were compressed with a hydraulic press at 10,000 psi for 2 min (Scheme 2B,C). Conversion of PUA@silica compacts to their carbonized products, referred to, in general, as C-PUA@silica, was carried out by direct heating at 800 °C under flowing ultra-high-purity Ar (Scheme 3A). Either under TGA in O_2 or after heating in a tube furnace at 1000 °C under flowing O_2, C-PUA-1.5×@silica, C-PUA-3×@silica, and C-PUA-4.5×@silica lost 64.0, 70.1, and 75.5% of their mass, respectively, corresponding to the amount of carbon in the composites; the balance was SiO_2. Data are summarized in Table 1. The data agree well with the compositions expected from the parent PUA@silica compacts given the carbonization yield of the TIPM-derived PUA (56% w/w).[28] Following the trend established by PUA in PUA@silica, the percent amount of carbon increased from 64 to 75.5% w/w with increasing the TIPM-to-silicon ratio in the cross-linking bath.

On the other hand, direct heating of PAN@silica compacts at 800 °C under Ar results in almost complete loss of the organic matter.[30] Conversion of PAN@silica compacts to their carbonized products requires prior oxidative ring-fusion aromatization of PAN (Scheme 3B).[33]

Scheme 3. Further Processing of PUA@silica and PAN@silica Compacts (See Scheme 1) toward Carbon Aerogels

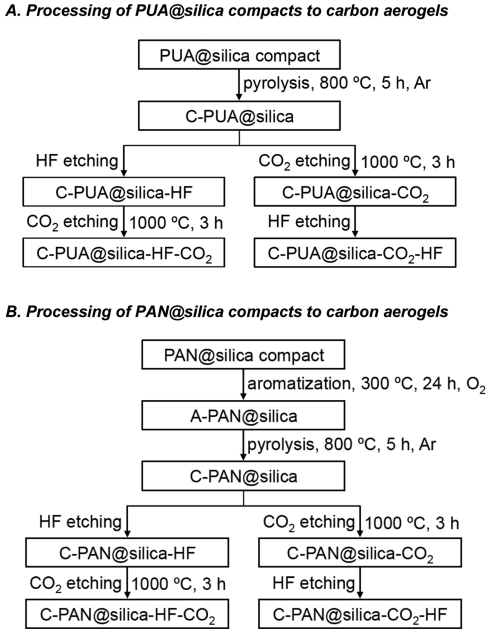

Modulated differential scanning calorimetry (MDSC) of PAN@silica compacts under O_2 (Figure 2) showed a strong exotherm in the 200−300 °C range with a maximum at 265 °C. Guided by the MDSC data, solid-state CPMAS ^{13}C NMR spectra of PAN@silica samples treated under various oxidative conditions showed that complete suppression of the aliphatic

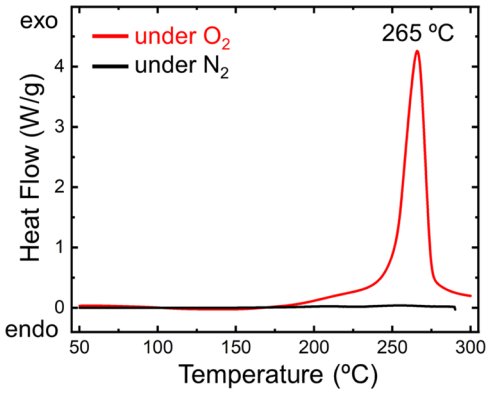

Figure 2. Typical modulated differential scanning calorimetry (MDSC) of PAN@silica samples demonstrated with PAN-6×@silica(9:1) under O_2 or N_2, as indicated (heating rate: 5 °C min^{-1}).

https://doi.org/10.1021/acs.chemmater.1c04170
Chem. Mater. 2022, 34, 4828−4847

Table 3. Mass Loss after Double Etching of Carbonized C-PUA@silica and C-PAN@silica Compacts[a]

Part A: The PUA@silica system			
	mass loss relative to the PUA@silica xerogel compacts [% w/w]		
sample	1.5×	3×	4.5×
C-PUA-*n*×@silica−HF−CO_2	88 ± 1	86 ± 1	87 ± 1
C-PUA-*n*×@silica−CO_2−HF	76 ± 2	79 ± 1	80 ± 2

Part B: The PAN@silica system				
	mass loss relative to the PAN@silica xerogel compacts [% w/w]			
sample	6×, (9:1)	2×, (9:1)	6×, (7:3)	2×, (7:3)
C-PAN-*n*×@silica(*x*:*y*)−HF−CO_2	73 ± 3	90 ± 1	76 ± 2	90 ± 1
C-PAN-*n*×@silica(*x*:*y*)−CO_2−HF	64 ± 3	80 ± 2	74 ± 1	79 ± 2

[a]Averages of three samples from three different batches at every composition.

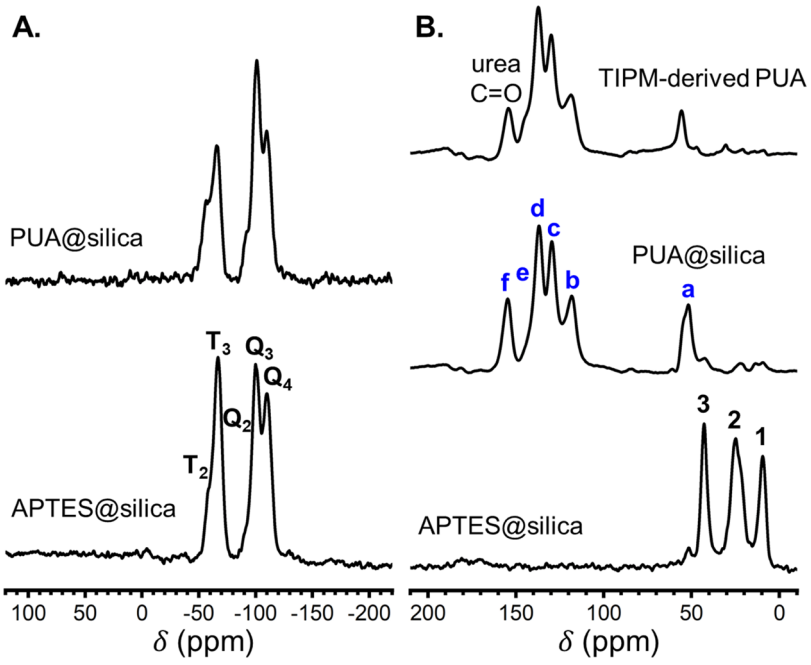

Figure 3. Solid-state CPMAS NMR spectra of representative PUA@silica samples (from the PUA4.5×@silica system) and of relevant controls: (A) ^{29}Si and (B) ^{13}C. For peak assignments, refer to Scheme 4. (The spectra of all three different compositions of the PUA@silica system are given in Figures S.4 and S.5 of Appendix III in the Supporting Information).

protons of PAN, at around 30 ppm, and thereby quantitative ring fusion aromatization, occurred only under prolonged treatment (24 h) at 300 °C in flowing O_2 (see Figure S.2 of Appendix II in the Supporting Information). Such aromatized PAN@silica compacts are referred to as A-PAN@silica (Scheme 3B). (The solid-state ^{13}C NMR spectra of the fully aromatized samples from all four compositions of the PAN@silica system are shown in Figure S.3 of Appendix II in the Supporting Information.)

Subsequently, A-PAN@silica samples were pyrolyzed at 800 °C for 5 h under flowing ultra-high-purity Ar and were converted to carbonized PAN@silica compacts, which are referred to, in general, as C-PAN@silica (Scheme 3B). Either under TGA in O_2 or after heating in a tube furnace at 1000 °C under flowing O_2, samples C-PAN-6×@silica(9:1), C-PAN-2×@silica(9:1), C-PAN-6×@silica(7:3), and C-PAN-2×@silica(7:3) lost 75.6, 46.5, 78.4, and 49.3% of their masses, respectively, corresponding to the amounts of carbon in the composites; the balance was SiO_2. Data are summarized in Table 2. The data agree well with the compositions expected from the parent PAN@silica compacts given the carbonization yield of PAN (70% w/w).[31,32] The expected compositions of the C-PAN@silica samples are included in Table 2. Following the trend established by PAN in PAN@silica, the percent amount of carbon increased with increasing the monomer ratio in the cross-linking bath (see Table 2).

2.1.4. Postcarbonization Processing of C-PUA@Silica and C-PAN@Silica Aerogels. Both carbonized products, C-PUA@silica and C-PAN@silica, were further treated with an aqueous HF solution at room temperature and with CO_2 gas at 1000 °C, in either order, i.e., either first with HF followed by high-temperature etching with CO_2 or first with flowing CO_2 gas at 1000 °C, followed by cooling back to room temperature and treatment with aqueous HF. The two treatments, and their sequence, are shown as extensions to the carbon aerogel names, for example, C-PAN-6×@silica(9:1)−CO_2−HF designates a carbon aerogel resulting from a first treatment of the specific C-PAN@silica aerogel with CO_2 at 1000 °C, followed by treatment with an aqueous HF solution; the carbon framework itself came from PAN-cross-linked silica prepared with a AN:total silicon ratio equal to 6:1 mol/mol, while silica had been formulated with a TMOS/APTES mol/mol ratio

https://doi.org/10.1021/acs.chemmater.1c04170
Chem. Mater. 2022, 34, 4828−4847

equal to 9:1. The HF treatment removed silica from the carbonized compacts, while etching with CO_2 increased the surface area and created microporosity by removing carbon. Curiously, the two treatments, first with HF or first with CO_2, were not equivalent in terms of their final effect. Although the processing conditions were identical, and both effective in terms of removing all silica (see Section 2.2.3), the materials treated first with HF displayed consistently a much higher overall mass loss than the samples treated first with CO_2 (Table 3). Given that the amount of silicon was the same in every pair of samples, the higher mass loss is attributed to a more efficient removal of carbon when silica was removed first.

2.2. Chemical Transformations along Processing. *2.2.1. PUA@Silica System.* The latching of APTES on TMOS-derived silica particles was confirmed with solid-state CPMAS ^{29}Si NMR (Figure 3A). The spectrum of APTES@silica shows a peak at −67 ppm with a shoulder at −59 ppm, which are assigned to the T_3 and T_2 silicon atoms from APTES, respectively, and two peaks at −110 ppm and at −101 ppm with a shoulder at −91 ppm, which are assigned to the Q_4, Q_3, and Q_2 silicon atoms of the TMOS-derived silica (see Scheme 4). The presence of the Q_3 and T_2 silicon atoms points to dangling Si−OH groups; thereby, APTES@silica offers two kinds of possible sites for the reaction with the isocyanate groups of TIPM: −OH and $-NH_2$.

Scheme 4. Two Ways of Latching of TIPM-Derived Polyurea on the Surface of Silica (through the $-NH_2$ Groups and through the −OH Groups)

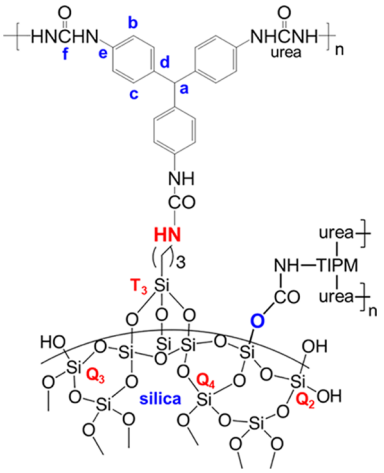

The CPMAS ^{13}C NMR spectrum of the APTES@silica powder (Figure 3B) shows the three $\underline{C}H_2$ resonances from APTES of about equal intensity at 43, 24, and 9.5 ppm. The spectrum of the PUA@silica powder was pretty similar to the spectrum of pure TIPM-derived polyurea (also included in Figure 3B for comparison).[34] For the peak assignment, refer to Scheme 4. Due to massive polymer uptake in PUA@silica, the relative intensity of the CH_2 groups from APTES is suppressed. Going back to the solid-state CPMAS ^{29}Si NMR spectra of Figure 3A, it is noted that the Q_3:Q_4 peak intensity ratio in PUA@silica is enhanced relative to its value in the spectrum of APTES@silica, indicating that triisocyanate (TIPM) was attached to the surface of the silica particles not only via the dangling $-NH_2$ groups of APTES but also via the innate −OH groups of silica resulting in urethane group formation, as summarized in Scheme 4.[20]

2.2.2. PAN@silica System. In addition to the Q_2, Q_3, and Q_4 peaks from silica, the CPMAS ^{29}Si NMR spectrum of initiator@silica (Figure 4A-bottom) shows peaks from the T_3 and T_2 silicon atoms of the APTES part of the initiator. Since the samples shown in Figure 4 were prepared with a TMOS/APTES mol ratio equal to 9:1, the relative intensity of the T-manifold in initiator@silica was lower than its intensity in APTES@silica, where the TMOS/APTES ratio was 4:1 (Figure 3A).

The solid-state CPMAS ^{13}C NMR spectrum of the initiator@silica powder (Figure 4B) includes the resonances from both APTES and ABCVA. Due to the massive polymer uptake, the solid-state ^{13}C NMR spectrum of the PAN@silica powder showed only the resonances assigned to PAN.

Going back to the solid-state CPMAS ^{29}Si NMR spectrum of PAN@silica (Figure 4A), it is noted that the T_3 peak is enhanced relative to its intensity in the spectrum of initiator@silica. This is attributed to the fact that the surface-bound radicals produced by homolytic cleavage of the initiator are still bound at the APTES sites, thereby PAN extends only from those points outward, as designed; the resulting close vicinity of the T_3 Si atoms to the protons of the developing polymer enhances cross-polarization (CP), and therefore the intensity of these silicon atoms increases due to more efficient excitation.

Oxidative aromatization of PAN@silica (see Section 2.2.2) was expected to leave the topographic relationship between the polymer and its anchoring sites more-or-less unperturbed, and indeed the ^{29}Si NMR spectra of A-PAN@silica and PAN@silica were practically identical (compare the middle and top spectra of Figure 4A). The solid-state ^{13}C NMR spectra of the PAN@silica samples treated at 300 °C for 24 h under O_2 (see Figure S.2 of Appendix II in the Supporting Information) were dominated by the resonances that correspond to the expected structure of fully aromatized PAN (refer to carbons 1′, 2′, and 3′ in Scheme 5); some lower-intensity resonances at around 170 ppm were assigned to pyridonic carbonyls (4′ and 4″); and lower-intensity resonances at around 102 ppm were assigned to sp^2 carbons on terminal rings (carbons 5′, 5″, 6′ in Scheme 5).

2.2.3. PUA@Silica- and PAN@Silica-Derived Carbons and Etched Carbons. Pyrolytic carbonization at 800 °C left both silica and carbon amorphous (by XRD); chemical analysis focused on the bulk elemental composition of the carbons before and after silica removal and reactive etching (using EDS), and most importantly for the intended application in CO_2 adsorption, on the functional groups present on the surfaces of the carbons (via XPS).

According to EDS (see Figure S.8 and Table S.1 of Appendix IV in the Supporting Information), in addition to C and N, carbonized C-PUA@silica and C-PAN@silica contained significant amounts of silicon and oxygen, for example, C-PUA-3×@silica and C-PAN-6×@silica(9:1) contained 13% (Si)/15% (O) w/w and 17% (Si)/16% (O) w/w, respectively. After treatment with HF, the amount of oxygen in C-PUA-3×@silica−HF and in C-PAN-6×@silica(9:1)−HF was reduced drastically to 2.3 and 2.7% w/w, respectively, and neither sample contained any silicon. Thereby, treatment with HF removed silica quantitatively. Both etched samples consisted of C, N, and O (no analysis was conducted for H).

High-resolution XPS for C, N, and O was conducted with carbonized samples to elucidate the functional groups; those elements are expressed with on the internal surfaces of the

https://doi.org/10.1021/acs.chemmater.1c04170
Chem. Mater. 2022, 34, 4828−4847

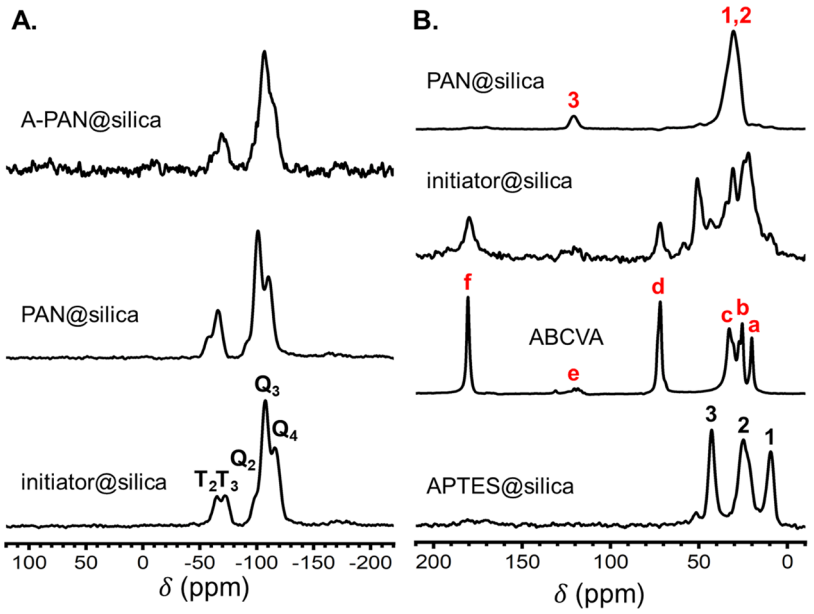

Figure 4. Solid-state CPMAS NMR spectra of representative PAN@silica samples (from the PAN-6×@silica(9:1) system) and of relevant controls: (A) ^{29}Si and (B) ^{13}C. For peak assignments, refer to Figure 1 and Scheme 5. (The spectra of all four compositions of the PAN@silica system are given in Figures S.6 and S.7 of Appendix III in the Supporting Information).

Scheme 5. Oxidative Conversion of PAN@silica Compacts to Aromatized PAN@silica Compacts (A-PAN@Silica)[a]

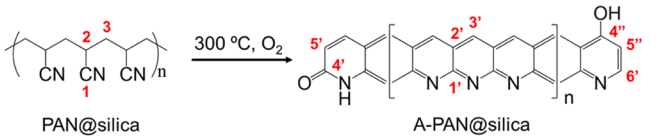

[a]The atom numbering is arbitrary and is used to facilitate discussion.

samples. Figures 5 and 6 show the O 1s and N 1s spectra of as-prepared C-PUA@silica and C-PAN@silica, respectively, and include the spectra of the corresponding double-etched C-PUA_or_PAN@silica−HF−CO_2. The XPS spectra of both as-prepared C-PUA@silica and of C-PAN@silica included a peak at 533.5 eV (see Figures 5A and 6A) and a peak at 103.6 eV (see Si 2p spectra in Figure S.9 of Appendix V in the Supporting Information). Both of those features are assigned to SiO_2.[35,36] Consistently with the EDS data, the Si 2p peak and the O 1s peak of silica were absent from the spectra of all

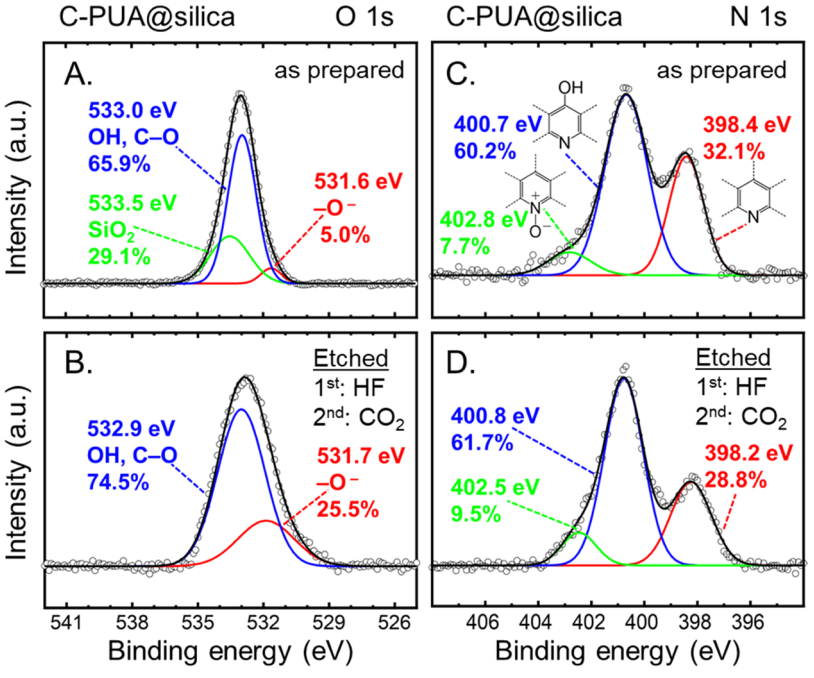

Figure 5. High-resolution O 1s (left) and N 1s (right) XPS spectra of: (A,C) C-PUA-4.5×@silica and (B,D) C-PUA-4.5×@silica−HF−CO_2. (For the Si 2p and C 1s spectra and those of the corresponding −CO_2−HF samples, see Figures S.9−S.12 of Appendix V in the Supporting Information).

https://doi.org/10.1021/acs.chemmater.1c04170
Chem. Mater. 2022, 34, 4828−4847

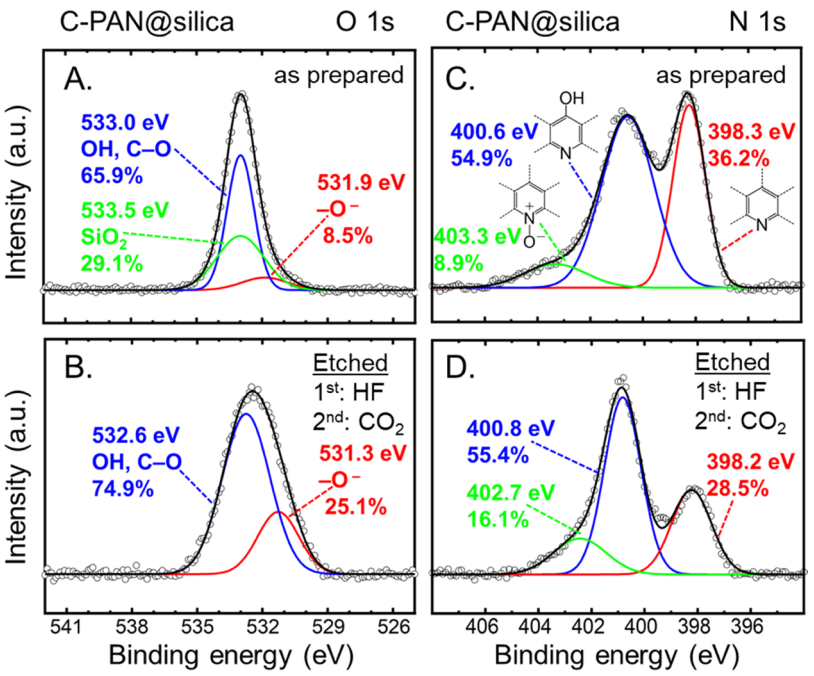

Figure 6. High-resolution O 1s (left) and N 1s (right) XPS spectra of: (A,C) C-PAN-6×@silica(9:1) and (B,D) C-PAN-6×@silica(9:1)−HF−CO_2. (For the Si 2p and C 1s spectra, and those of the corresponding $-CO_2-HF$ samples, see Figures S.9−S.12 of Appendix V in the Supporting Information).

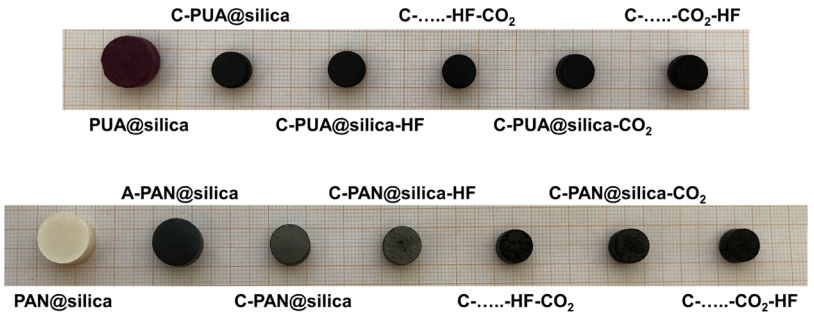

Figure 7. Photographs of PUA-3×@silica and PAN-6×@silica (9:1) compacts, abbreviated as PUA@silica and PAN@silica, respectively, along carbonization and etching.

samples, double etched in either sequence (see Figures 5B, 6B, and S.10 of Appendix V in the Supporting Information).

Also, the O 1s spectra of as-prepared C-PUA@silica and of C-PAN@silica (Figures 5A and 6A) contained a strong peak at 533.0 eV that falls in the middle of the range of and can be assigned to either OH (e.g., from pyridone) or ether/ester C−O, and lower-intensity peaks at 531.6 and 531.9 eV, respectively, which can be assigned to C═O, but they can also be attributed to $-O^-$.[37−39] We opted for the latter assignment because of the presence of nitroxide in the N 1s spectra. Indeed, the N 1s spectra of C-PUA@silica and C-PAN@silica (see Figures 5C and 6C) showed N mainly in pyridinic (398.3−398.4 eV) and pyridonic positions (400.6−400.7 eV; more pyridonic in C-PUA@silica than in C-PAN@silica) and small amounts of nitroxide at 402.8 eV (case of C-PUA@silica) or at 403.3 eV (case of C-PAN@silica).[39−42]

The O 1s spectra of double-etched carbon samples contained the same OH/C−O, and $-O^-$ peaks, but the intensity of the $-O^-$ peak at ∼532 eV increased significantly relative to before etching—from 5 to 25.5% (case of C-PUA@silica−HF−CO_2) and from 8.5 to 25.1% (case of C-PAN@silica−HF−CO_2). Simultaneously, the intensity of the N 1s peaks attributed to pyridonic and nitroxide ($-N^+-O^-$) also increased; the first marginally, the second significantly. For example, the intensity of the N 1s assigned to nitroxide went from 7.7 to 9.5% (case of C-PUA@silica−HF−CO_2—compare Figure 5C5 and 5D) and from 8.9 to 16.1% (case of C-PAN@silica−HF−CO_2—compare Figure 6C and 6D).

Similar evolutions in the O 1s and N 1s spectra were observed in double-etched C-PUA_or_PAN@silica−CO_2−HF samples (see Figures S.10 and S.11 of Appendix V in the Supporting Information). The C 1s spectra (see Figure S.12 of Appendix V in the Supporting Information) were consistent with the functional groups identified from the O 1s and N 1s spectra, showing peaks at 284.5 eV (aromatic C), 285.3 eV (C═N), and at 287−288 eV (very broad) for carbon in both straight C═O groups and in C═O groups participating in a keto/enol equilibrium (e.g., as in pyridonic groups).[43−45]

2.3. Evolution of Materials Properties along Processing. *2.3.1. Bulk Material Properties of PUA@Silica, PAN@Silica, and Their Carbons.* Figure 7 shows typical PUA@silica and PAN@silica compacts along processing. The compacts were prepared with the same die and had the same dimensions. The photographs show that the compacts developed no

https://doi.org/10.1021/acs.chemmater.1c04170
Chem. Mater. 2022, 34, 4828−4847

defects, and the two series of samples were practically indistinguishable at the same stages of processing. Relevant property characterization data for all materials and all formulations considered in this study are summarized in Tables S.3 and S.4 of Appendix VI in the Supporting Information.

The bulk density (ρ_b) of PUA@silica xerogel compacts was in the range of 0.894−1.007 g cm^{-3}; the skeletal density (ρ_s) was in the range of 1.332−1.369 g cm^{-3}. Both ρ_b and ρ_s decreased as the amount of PUA in the composite increased (Table S.3).

The bulk density (ρ_b) of PAN@silica xerogel compacts was in the range of 1.282−1.441 g cm^{-3}, while the skeletal density (ρ_s) was in the range of 1.182−1.373 g cm^{-3}. The trends in ρ_b and ρ_s as a function of the amount of PAN were similar to those in PUA@silica.

The operation of squeezing the void space out of PAN@silica compacts was more effective than in PUA@silica. The percent open porosity, Π, calculated from bulk and skeletal density data via $\Pi = 100 \times (\rho_s - \rho_b)\ \rho_s$, was in the range of 26−33% v/v for PUA@silica xerogel compacts and only 5−7% v/v for PAN@silica xerogel compacts. The carbonization process of PUA@silica xerogel compacts brought about a linear shrinkage of about 28% for all samples; yet, because of the mass loss, the porosity increased into the 38−51% v/v range. For PAN@silica xerogel compacts, the aromatization process brought about a linear shrinkage of 9 ± 3% and a slight-to-moderate increase in porosity into the range of 8−24% v/v. The subsequent carbonization of A-PAN@silica compacts resulted in a total linear shrinkage of up to 22%, and an increase in porosity into the 22−32% v/v range. Overall, although the loss of mass due to the carbonization process did create some void space, the porosity never exceeded 51% v/v (case of C-PUA@silica), while in C-PAN@silica, the porosity remained significantly lower and never exceeded the 32% v/v mark under our conditions.

In contrast, the subsequent etching processes with HF and CO_2, and especially their sequence, had a profound effect on the porosity, surface areas, and pore size distribution.

After the first etching of C-PUA@silica compacts with HF, ρ_b and ρ_s decreased as expected from the fact that silica was removed. Samples did not shrink further, and the porosities of C-PUA@silica−HF were higher (in the 54−63% v/v range) relative to those of C-PUA@silica (38−51% v/v). On the other hand, when C-PUA@silica samples were etched with CO_2 first, linear shrinkage increased somewhat, which apparently compensated for the mass loss, and ρ_b remained about the same; ρ_s, however, increased consistent with removing carbon while silica stayed behind. The porosities of C-PUA@silica−CO_2 were slightly higher (39−56% v/v) than those of C-PUA@silica (38−51% v/v) and slightly lower than those of C-PUA@silica−HF (54−63% v/v).

What was remarkable at this point though was that further etching of C-PUA@silica−HF with CO_2 propelled the porosity of the resulting C-PUA−silica−HF−CO_2 into the 82−83% v//v range (from 54 to 63% v/v). On the contrary, the porosity of the C-PUA−CO_2−HF samples remained significantly lower, in the 62−74% v/v range. Meanwhile, the shrinkages of all double-etched samples converged to the level noted for the samples etched first with CO_2 (i.e., of C-PUA@silica−CO_2). (For all specific values, refer to Tables S.3 and S.4 in the Supporting Information.)

After HF-etching, C-PAN@silica compacts shrank by about an additional 5% in linear dimensions; nevertheless, both ρ_b and ρ_s decreased due to the removal of silica (refer to Table S.4). The porosities of C-PAN@silica−HF were higher (in the 35−64% v/v range) relative to those of C-PAN@silica (22−32% v/v). Consistent with what was found out by etching of C-PUA@silica, if C-PAN@silica is first etched with CO_2, the shrinkage is higher (by about an additional 25%) and the porosity is lower (in the 29−51% v/v range) than the porosity of the carbon samples etched first with HF (in the 35−64% v/v range). A second etching step with CO_2, or HF, respectively, equalized the shrinkages and consistent with what was found with double etching of the C-PUA@silica samples; the porosities of the samples etched with HF first, i.e., of C-PAN@silica−HF−CO_2, were significantly higher (in the range of 61−82% v/v) than the porosities of the C-PAN@silica−CO_2−HF (in the 57−74% v/v range).

The differences in the porosities of the terminal carbons as a function of the sequence of treatment with HF versus CO_2 were also accompanied by differences in the pore structure and surface areas.

2.3.2. Nanostructure of Carbon Aerogels from PUA@silica and PAN@silica Compacts and a Model for the Etching Processes. Microscopically (SEM), cleaved surfaces of all PUA@silica and PAN@silica compacts were featureless. Some unevenness appeared after carbonization. Voids and other formations at the submicron level were generated after etching with HF and CO_2; the newly exposed surfaces were smooth, but bumps, e.g., from fused spherical nanoparticles about 100 nm in diameter or less, were clearly visible. Those changes are illustrated in Figure 8 using C-PAN-6×@silica(9:1) and its double-etched derivatives as an example. After CO_2 removal and etching, the samples resembled other carbon aerogels, most notably polybenzoxazines.[7] The definite conclusion from SEM imaging though was that the etching processes generated macroporosity; however, owing to the apparent smoothness of the macroporous surfaces, it was decided to rely on N_2 sorption as a higher-resolution probe of the pore structure in the meso- and micropore size regimes.

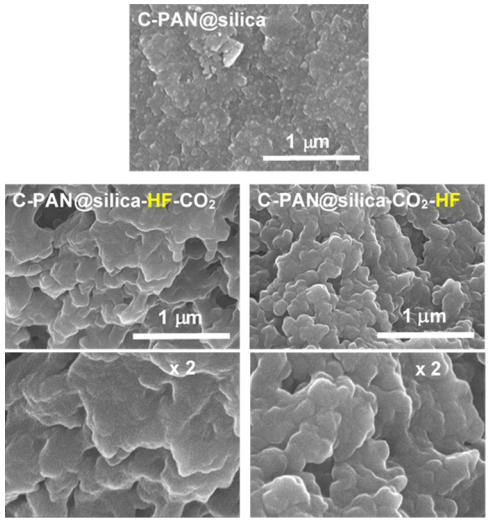

Figure 8. Typical SEM images along processing represented by carbonized C-PAN-6×@silica(9:1) and its double-etched derivatives at two different magnifications, as indicated. (The etching process that is applied first is highlighted yellow in the material's name).

https://doi.org/10.1021/acs.chemmater.1c04170
Chem. Mater. 2022, 34, 4828−4847

The evolution of the N_2-sorption isotherms of C-PUA@silica and C-PAN@silica upon further treatment with HF and then CO_2 or with CO_2 and then HF is shown in Figures 9 and 10, respectively. Both systems follow the same pattern. To begin with, the adsorption of N_2 by either C-PUA@silica or C-PAN@silica was negligibly small, suggesting that the porosities reported above (38−51 and 22−32% v/v, respectively) corresponded to macropores with >300 nm in diameter. Things changed when the first etching process was conducted with HF rather than CO_2. In both cases, the N_2 uptake increased, but only the isotherms of C-PUA@silica−HF and C-PAN@silica−HF showed the characteristic hysteresis loops of mesoporosity; on the contrary, in both types of materials, a first treatment with CO_2 yielded only a sharp rise of the isotherms at low pressures, characterizing microporosity, and no hysteresis loops from mesoporosity (cases of C-PUA@silica−CO_2 and C-PAN@silica−CO_2). Indeed, BJH analysis of the desorption branches of the isotherms of all four singly etched carbons (i.e., of C-PUA@silica−HF or −CO_2 and C-PAN@silica−HF or −CO_2) yielded meaningful pore size distributions in the mesopore range only for C-PUA@silica−HF and C-PAN@silica−HF (see insets in Figures 9 and 10). Subsequent treatment with the second etching agent resulted in materials with N_2-sorption isotherms, indicating the presence of both mesopores and micropores, irrespective of their origin. The BJH plots of all four terminal doubly etched materials show similar pore size distributions centered at similar pore diameters, a little less than 10 nm; the distribution maxima were at slightly higher values in materials etched first with HF (blue lines—see Figure 11). A final note on the isotherms is that the shape of the desorption branches of all C-PAN@silica−HF, −HF−CO_2, and −CO_2−HF indicates ink-bottle types of mesopores. That kind of shape was not as well defined in the corresponding cases of the PUA-derived samples.

Consistently, the total volume of N_2 uptaken by samples etched first with HF, that is C-PUA@silica−HF−CO_2 and C-PAN@silica−HF−CO_2, was significantly higher than that of C-PUA@silica−CO_2−HF and C-PAN@silica−CO_2−HF. That behavior matched the trends in the porosity as described in the previous section and is also reflected in the corresponding surface areas (refer to Tables S.3 and S.4 in the Supporting information). Specifically, the BET surface areas of C-PUA@silica and C-PAN@silica were very low (1.3−11.0 and 0.47−7.9 $m^2\ g^{-1}$, respectively). Upon treatment with HF, the BET surface area of C-PUA@silica−HF jumped in the 285−394 $m^2\ g^{-1}$ range (20% assigned to micropores), while the BET surface area of C-PAN@silica−HF jumped in the 193−618 $m^2\ g^{-1}$ range (5−20% was assigned to micropores). On the other hand, first etching with CO_2 increased the surface areas of the corresponding samples roughly up to the same range as the HF

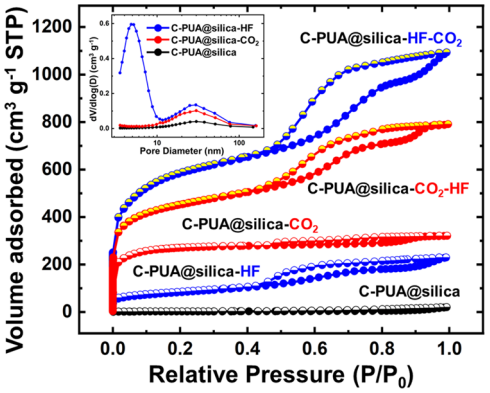

Figure 9. N_2-sorption isotherms at 77 K of carbonized C-PUA-4.5×@silica compacts after each processing step. (Inset: BJH pore size distributions for the lower three isotherms according to their color coding).

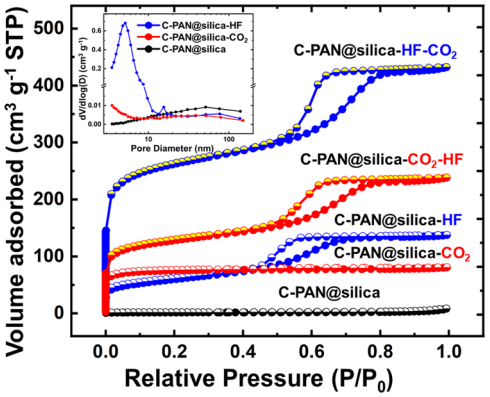

Figure 10. N_2-sorption isotherms at 77 K of carbonized C-PAN-6×@silica-(9:1) compacts after each processing step. (Inset: BJH pore size distributions for the lower three isotherms according to their color coding).

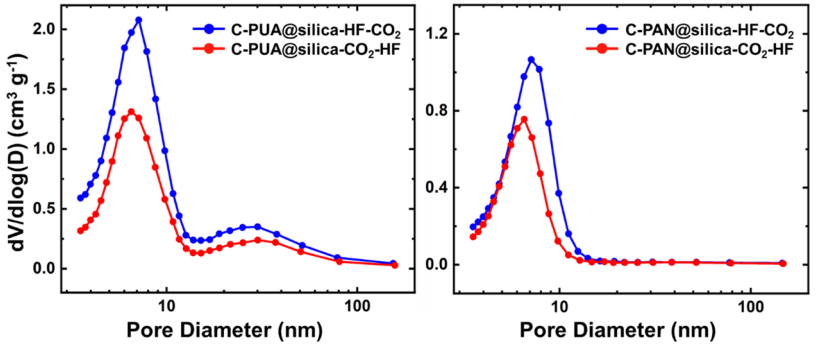

Figure 11. Pore-size distributions using the BJH desorption method of carbonized and double-etched compacts: C-PUA-4.5×@silica (left) and C-PAN-6×@silica(9:1) (right). The etching sequence is color coded as shown in the legends inside the frames: HF−CO_2 in blue versus CO_2−HF in red.

https://doi.org/10.1021/acs.chemmater.1c04170
Chem. Mater. 2022, 34, 4828−4847

treatment; however, in the case of C-PUA@silica−CO_2, over 70% of the new surface area was assigned to micropores and 50−80% in the case of C-PAN@silica−CO_2.

Treatment with the second etching agent propelled BET surface areas up to 1930 $m^2\ g^{-1}$ (case of C-PUA-4.5×@silica−HF−CO_2), 37% of which was assigned to micropores, and up to 1433 $m^2\ g^{-1}$ (22% assigned to micropores—case of C-PAN-2×@silica(9:1)−HF−CO_2). For reference and further analysis by the interested reader, complete data for all samples are presented in Tables S.3 and S.4 in the Supporting Information.

The pore structure of the double-etched samples was also probed with low-pressure N_2-sorption using a low-pressure transducer. The derived micropore volumes, $V_{micropore}$, are included in Tables S.3 and S.4 of Appendix VI in the Supporting Information. In all cases, $V_{1.7-300\_nm} + V_{micropore} < V_{Total}$ (V_{Total} was calculated from bulk and skeletal density data via $V_{Total} = (1/\rho_b) - (1/\rho_s)$), meaning that, in agreement with conclusions drawn from SEM, all samples included a certain amount of macropores with sizes >300 nm. A second observation is that, in general, $V_{micropore}$ were lower in samples etched first with CO_2.

Overall, percent mass loss, porosity values (Π), specific pore volumes V_{Total} and $V_{micropore}$, and BET surface areas were higher in double-etched samples that were treated first with HF. Since the etching action of CO_2 is a comproportionation reaction with C to yield 2 CO, it is reasonable to suggest that silica protects the carbon it is in contact with. As illustrated in Scheme 6, if silica is removed first, more surface area of carbon becomes accessible to the etching effect of CO_2.

Scheme 6. Etching Model of Carbonized C-PUA@silica and C-PAN@silica with HF and CO_2 in Either Sequence[a]

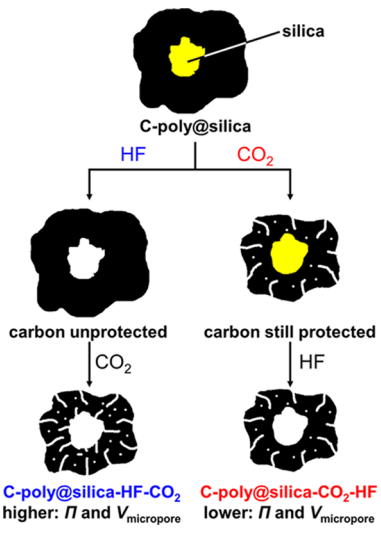

[a]poly = PUA or PAN; micropores are shown as white wiggly lines penetrating into the bulk of carbon.

2.4. Probing Microporosity with CO_2 and Application of Doubly Etched PUA@silica- and PAN@silica-Derived Carbon Aerogels to Highly Selective CO_2 Capture. Conventional carbon aerogels with micropores lined with O and N have shown a high capacity for CO_2 adsorption.[1,8] Since this property has a clearly defined application in CO_2 sequestration, it was considered as a basis for comparison with conventional carbon aerogels, namely, carbon aerogels obtained via pyrolysis of polymeric aerogels. CO_2 adsorption isotherms at two different temperatures (273 and 298 K) and up to 1 bar (corresponding to partial pressure $P/P_0 = 0.03$) of all double-etched, in either sequence, carbon samples of this study are shown in Figure 12. All isotherms were reversible with no hysteresis. By cross-referencing the data of Figure 12 with other material properties from Tables S.3 and S.4, maximum CO_2 uptake was observed with the lower-density, higher-porosity, higher micropore volume, and lower micropore surface area samples, namely, with C-PUA-4.5×@silica−HF−CO_2 (9.15 mmol g^{-1}) and C-PUA-4.5×@silica−CO_2−HF (6.13 mmol g^{-1}), as well as with C-PAN-2×@silica(7:3)−HF−CO_2 (6.56 mmol g^{-1}) and C-PAN-2×@silica(7:3)−CO_2−HF (5.30 mmol g^{-1}). PAN-derived carbon aerogels adsorbed lower amounts of CO_2 than their PUA-derived analogues. Also, a lower CO_2 uptake was observed with samples obtained through the CO_2/HF etching sequence relative to their counterparts obtained through the HF/CO_2 sequence. Figure 13 compares the maximum CO_2 uptake by the best samples in the four groups of this study (PUA versus PAN and −HF−CO_2 versus −CO_2−HF) with other CO_2 adsorbers from the literature. Overall, most samples displayed levels of CO_2 uptake that were among what has been observed before with other carbon aerogels (around 5−6 mmol g^{-1}).[1] By the same token, however, the best performer of this study, C-PUA-4.5×@silica−HF−CO_2 (9.15 mmol g^{-1}), was above the best performers in the literature (e.g., phenolic resin-based activated carbon microspheres[46] or carbon nanotube superstructures),[47] yet lower than certain CO_2-etched carbon aerogels from pyrolysis of low-density resorcinol-formaldehyde (RF) aerogels, which have shown CO_2 uptake up to 14.8 ± 3.9 mmol g^{-1}.[1] Unfortunately, the excellent performance of those RF-derived carbon aerogels was compromised by their low gravimetric density and the low yield of the etching process. C-PUA-4.5×@silica−HF−CO_2 does not have this problem and in addition its preparation bypasses all of the expensive steps of aerogel synthesis.

The involvement of the micropores in the CO_2 uptake was investigated by comparing the experimental CO_2 uptake with values calculated by assuming three different scenarios: (a) monolayer coverage of the entire BET surface area with CO_2 (using the value of 0.17 nm^2 per molecule);[48] (b) monolayer coverage of only the micropore surface area; and (c) micropore volume filling with CO_2 in a state that resembles liquid CO_2 (density of that state = 1.023 g cm^{-3}).[49,50] Micropore volumes were calculated using either the Dubinin−Radushkevich (DR) method on low-pressure N_2-sorption data at 77 K and on CO_2 adsorption data at 0 °C or the density functional theory (DFT) method on the CO_2 adsorption data at 0 °C. All relevant data are summarized in Table 4. It is noted, however, that since the DR(CO_2) volumes and the reported amount of CO_2 uptaken are not values independent of one another, the DR(CO_2) volumes were not considered in calculating the pore filling with CO_2; instead, they were used for comparing the pore volumes calculated via the DR(N_2) method. Oftentimes, these two micropore volumes agree with one another, which are taken to mean that in these cases CO_2 fills the "micropores." Subsequently, both the DR(N_2) and the DR(CO_2) values were used for calculating average "micropore" sizes. ("Micropore" here is used broadly and refers to pores falling in the range between large micropores and small mesopores as probed by CO_2 or low-pressure N_2 sorption and identified by the DR method.)

https://doi.org/10.1021/acs.chemmater.1c04170
Chem. Mater. 2022, 34, 4828−4847

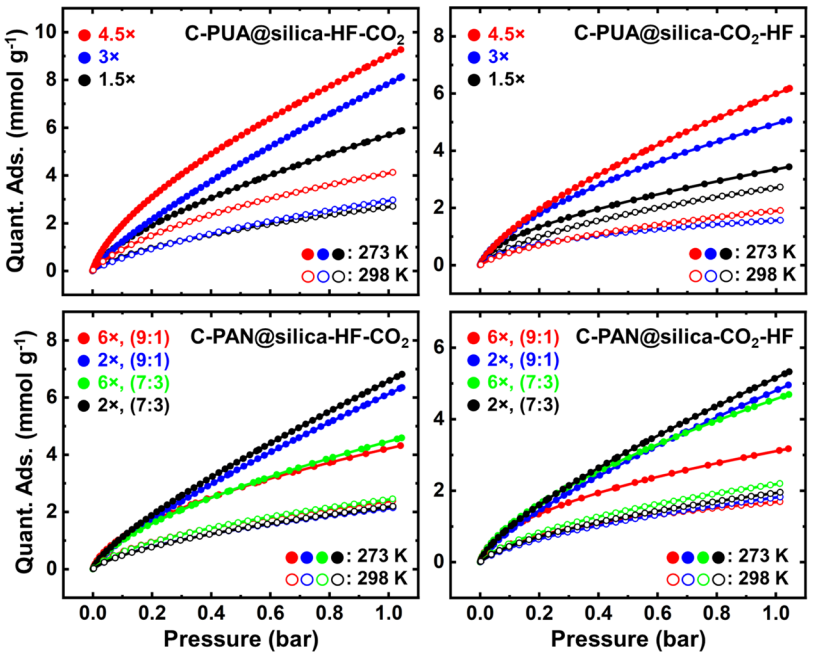

Figure 12. CO_2 adsorption isotherms of all etched carbon aerogels of this study at two different temperatures as shown. (For clarity, only the adsorption branches are shown, but all isotherms were reversible without hysteresis).

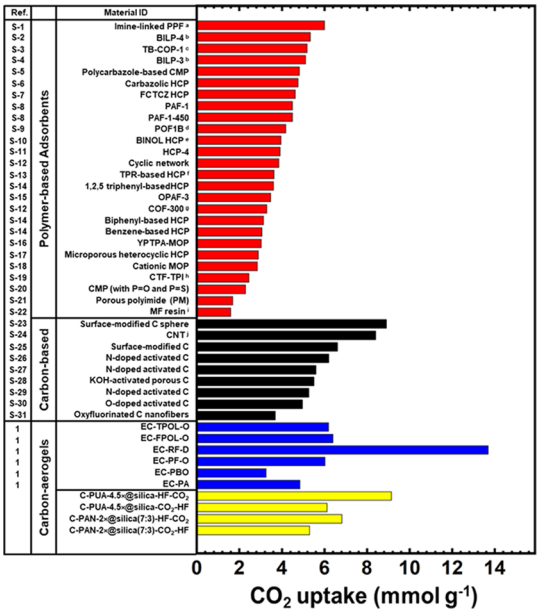

Figure 13. Comparison of CO_2 uptake at 1 bar/273 K by the carbon aerogel materials of this study (yellow bars) with similar materials from previous studies by our group (blue bars—reference No. 1) and other superior-CO_2 sorbents from the literature. Selected abbreviations: [a]PPF: porous polymer framework; [b]benzimidazole-linked polymers; [c]Tröger's base COP; [d]polymeric organic framework; [e]binaphthol-based HCP; [f]tetraphenylethylene-based HCP; [g]covalent organic framework; [h]covalent triazine framework; [I]melamine-formaldehyde resin; and [j]carbon nanotube. For the corresponding references, refer to Appendix VII in the Supporting Information.

As it can be seen in Table 4, the amounts of CO_2 uptaken at the highest points of the isotherms of Figure 12 are bracketed from above by the calculated amount of CO_2 required to provide monolayer coverage of the entire BET surface areas and from below by the amount of CO_2 required to fill the volumes calculated by the DFT method of pores with sub-nanometer pore sizes. Specifically for the latter, independently of the polymer system or the etching sequence, all double-etched materials showed similar micropore size distributions by the DFT method applied on the CO_2 adsorption isotherms (see Figure S.13 of Appendix VIII in the Supporting Information) and similar specific micropore volumes (all around 0.08−0.12 $cm^3\ g^{-1}$)—see Table 4; filling those DFT-derived micropore volumes with CO_2 typically requires only 2−3 mmol g^{-1} of CO_2, exception being the case of C-PUA-4.5×@silica−HF−CO_2 that requires 4.2 mmol g^{-1}; yet in all cases, the amount of CO_2 required to fill those DFT-derived micropore volumes was much below the experimentally observed values of CO_2 uptake (Table 4). Necessarily then, CO_2 adsorption should be correlated with structural features falling between the two extremes (the BET surface area and the DFT micropore volume).

Indeed, as summarized in Figure 14, it is observed that whenever the average micropore diameter from the DR(N_2) and DR(CO_2) methods was approximately 3−4 nm, the amount of CO_2 uptaken was near the amount required for monolayer coverage of the micropores. When the average micropore diameter was <3 nm, the amount of CO_2 uptaken was less, to significantly lesser than what was required for monolayer coverage of the micropores; when the average micropore diameter was >4 nm, the CO_2 uptaken was more, to significantly more than the amount required for monolayer coverage of the micropores, yet it always remained less than the amount of CO_2 required to fill the "micropore" volumes that were calculated with the DR(N_2) method. In other words, CO_2 seems to fill all sub-nanometer micropores (accounted for by the DFT(CO_2) method) and continues to cover the surfaces of small pores falling in the region between what is still defined formally as micropores and the small end of mesopores. In that region, there appears to be a pore-size threshold (in the 3−4 nm range), below which micropores are not coated with CO_2 completely, and above which CO_2 keeps

https://doi.org/10.1021/acs.chemmater.1c04170
Chem. Mater. 2022, 34, 4828−4847

Table 4. Micropore Analysis and CO_2 Uptake at 0 °C by All Carbonized and Double-Etched Xerogel Compacts

							CO_2 uptake [mmol g^{-1}] at 273 K, 1 bar				
	specific micropore volume [cm^3 g^{-1}]			micropore diameter [nm] via $4 \times V/$(micropore area)[d]				calculated from			
								monolayer coverage of surface areas		filling micropore volumes	
sample	DR(N_2)[a]	DR(CO_2)[b]	DFT(CO_2)[c]	V from DR(N_2)	V from DR(CO_2)	average[e]	measured experimentally	BET[f]	Micropore[g]	DR(N_2)[h]	DFT(CO_2)[h]
					C-PUA@silica−HF−CO_2						
1.5×	0.74	0.43 ± 0.01	0.11 ± 0.01	4.71	2.74 ± 0.07	3.73	5.75 ± 0.17	12.5	6.1	17.2	2.6 ± 0.1
3×	0.75	0.64 ± 0.03	0.12 ± 0.01	4.24	3.64 ± 0.15	3.93	7.98 ± 0.15	16.8	6.9	17.4	2.7 ± 0.1
4.5×	0.86	0.69 ± 0.01	0.18 ± 0.01	4.86	3.91 ± 0.05	4.38	9.15 ± 0.10	18.9	6.9	20.0	4.2 ± 0.1
					C-PUA@silica−CO_2−HF						
1.5×	0.21	0.23 ± 0.01	0.08 ± 0.01	1.26	1.49 ± 0.04	1.32	3.34 ± 0.10	11.2	6.5	4.9	1.8 ± 0.1
3×	0.42	0.38 ± 0.01	0.12 ± 0.01	2.67	2.27 ± 0.03	2.54	5.13 ± 0.09	11.9	6.2	9.8	2.7 ± 0.1
4.5×	0.62	0.48 ± 0.02	0.08 ± 0.03	4.06	2.74 ± 0.17	3.60	6.13 ± 0.07	13.0	6.0	14.4	2.0 ± 0.4
					C-PAN@silica−HF−CO_2						
6×, (9:1)	0.37	0.30 ± 0.01	0.11 ± 0.01	3.01	2.46 ± 0.07	2.73	4.34 ± 0.11	8.2	4.8	8.6	2.6 ± 0.1
2×, (9:1)	0.60	0.52 ± 0.02	0.10 ± 0.01	7.43	6.39 ± 0.05	6.93	6.68 ± 0.29	14.0	3.2	14.0	2.3 ± 0.1
6×, (7:3)	0.42	0.35 ± 0.01	0.11 ± 0.01	3.14	2.58 ± 0.04	2.88	4.78 ± 0.14	10.0	5.2	9.8	2.5 ± 0.1
2×, (7:3)	0.56	0.50 ± 0.02	0.10 ± 0.01	6.07	5.43 ± 0.22	5.75	6.82 ± 0.12	13.9	3.6	13.0	2.4 ± 0.1
					C-PAN@silica−CO_2−HF						
6×, (9:1)	0.29	0.30 ± 0.01	0.08 ± 0.01	5.42	5.65 ± 0.16	5.51	3.05 ± 0.09	4.1	2.1	6.7	1.9 ± 0.1
2×, (9:1)	0.42	0.38 ± 0.02	0.08 ± 0.01	6.36	5.78 ± 0.35	6.06	5.11 ± 0.27	11.4	2.6	9.8	1.9 ± 0.1
6×, (7:3)	0.44	0.33 ± 0.01	0.10 ± 0.01	3.90	2.95 ± 0.06	3.41	4.60 ± 0.08	9.7	4.4	10.2	2.3 ± 0.1
2×, (7:3)	0.43	0.39 ± 0.01	0.09 ± 0.01	6.54	5.86 ± 0.020	6.24	5.30 ± 0.12	11.2	2.6	10.0	2.1 ± 0.1

[a]Via the Dubinin−Radushkevich (DR) method from N_2-sorption data obtained at 77 K using a low-pressure transducer ($P/P_0 \leq 0.01$). Single experiment. [b]Via the DR method from CO_2 adsorption data at 273 K up to relative pressure of 0.015. [c]Using the same data as in footnote (b) and applying the DFT method. Pore volumes correspond to pores <1 nm in size. [d]Calculated as indicated using the micropore surface areas obtained from N_2-sorption data via the t-plot method. [e]Calculated via $4 \times V/$(micropore area), where $V = [V_{DR(N2)} + V_{DR(CO2)}]/2$. [f]Calculated by dividing the BET surface area over the CO_2 cross-sectional area (0.17 nm^2),[48] over the Avogadro's number. [g]Calculated by dividing the micropore surface area obtained from N_2-sorption data via the t-plot method over the CO_2 cross-sectional area (0.17 nm^2), over Avogadro's number. [h]Calculated by assuming that micropore volumes (via the DR(N_2) and the DFT(CO_2) methods—see footnotes a and c, respectively) are filled with liquid CO_2 (the density of liquid CO_2 at 273 K was taken equal to the density of adsorbed CO_2 (1.023 g cm^{-3})).[49,50] Errors were calculated by applying rules of propagation of error.

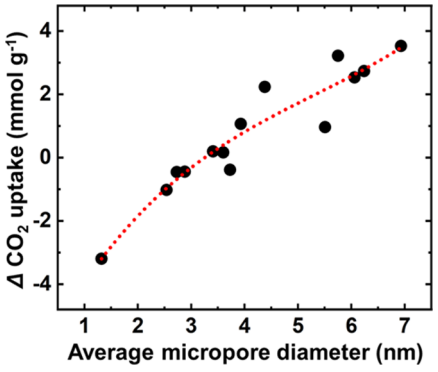

Figure 14. Differential (Δ: experimental minus expected) CO_2 uptake versus average micropore diameter for all carbonized and double-etched, by either sequence, PUA@silica, and PAN@silica xerogel compacts. The experimental CO_2 uptake was taken from the maximum of the isotherms in Figure 12. The expected CO_2 uptake was calculated from micropore monolayer coverage (see footnote "g" in Table 4). Average micropore diameters were calculated as described in footnote "e" of Table 4. The dotted line is a third-order polynomial fit.

on accumulating on already adsorbed CO_2 but never fills those small mesopores completely. It is speculated that in both cases the ultimate amount of CO_2 uptaken is controlled by the fact that the entropic penalty of new CO_2 molecules entering the small pores can no longer be ignored.[51]

Further insight into the interaction of CO_2 with the surface of the carbon aerogels was obtained by calculating the isosteric heats of adsorption of CO_2 (Q_{st}) by the four doubly etched carbon aerogels with the highest CO_2 uptake capacities among their peers: C-PUA-4.5×@silica−HF−CO_2 and −CO_2−HF; C-PAN-2×@silica(7:3)−HF−CO_2 and −CO_2−HF. Q_{st} is defined as the negative of the differential change in the total enthalpy of a closed system, and values were calculated as a function of the CO_2 uptake using simultaneous Virial fitting on the CO_2 adsorption isotherms at two different temperatures (273 and 298 K—see Section 4 and Table S.5 in Appendix IX of the Supporting Information). The plots of the Q_{st} values of the four materials versus the CO_2 uptake are shown in Figure 15. The intercept of any Q_{st} plot at zero CO_2 uptake is referred to as Q_0 and is the energy of interaction of CO_2 with the surface of the adsorber. In general, Q_0 values >40 kJ mol^{-1} are generated by chemisorption, while lower values by physisorption.

The Q_0 values of the four double-etched samples, C-PUA-4.5×@silica−HF−CO_2 and −CO_2−HF; C-PAN-2×@silica(7:3)−HF−CO_2 and −CO_2−HF, were in the range of 27−32 kJ mol^{-1} (see Table S.6 of Appendix IX in the Supporting Information). Those values can be attributed to either weak chemisorption or strong physisorption, and their numerical proximity reflects the fact that irrespective of the polymeric origin of the carbons implemented in this study, or their etching sequence, the surfaces of all four systems are lined with the same functional groups (refer to the XPS data in

https://doi.org/10.1021/acs.chemmater.1c04170
Chem. Mater. 2022, 34, 4828−4847

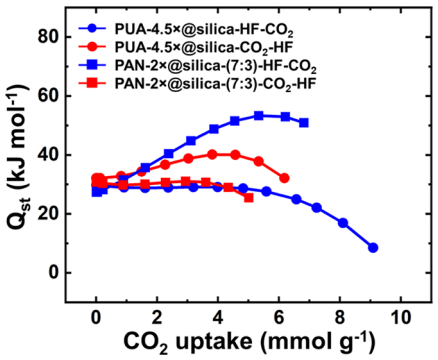

Figure 15. Isosteric heats of CO_2 adsorption of the four samples of this study with the highest CO_2 uptakes as a function of the latter. (For clarity, only one of every four points is shown).

Section 2.2.3 above, and in Appendix V of the Supporting Information). Physisorption may involve quadrupolar interactions between quadrupolar CO_2 and quadrupolar nitrogen-rich sites.[52] Those interactions are favored in smaller micropores (yielding higher Q_0 values),[53] where quadrupolar fields come closer to one another and may interact better with the adsorbate.[54,55] On the other hand, a special kind of weak chemisorption of CO_2 on the surface of carbon may involve nucleophilic attack of surface $-O^-$ (for example, from nitroxides) and $-N:$ (for example, from pyridinic and pyridonic sites) onto CO_2 yielding surface-bound carbonate or carbamate, respectively. The reaction of CO_2 with surface $-O^-$ is nearly isoenthalpic, while its reaction with $-N$ is slightly endothermic.[1,8]

Since the micropore volume of PUA-4.5×@silica−HF−CO_2 according to the DR(N_2) method is larger (0.86 $cm^3\ g^{-1}$) than the micropore volume of C-PAN-2×@silica(7:3)−CO_2−HF (0.43 $cm^3\ g^{-1}$), filling of the former requires more CO_2 than filling of the latter, thus resulting in 9.15 mmol g^{-1} versus 5.30 mmol g^{-1} of CO_2 uptake, respectively.

On the other hand, in the case of double-etched carbon aerogels with N-rich surfaces, i.e., C-PUA-4.5×@silica−CO_2−HF and C-PAN-2×@silica(7:3)−HF−CO_2, the micropore volume of the latter is less (0.37 $cm^3\ g^{-1}$) than that of the former (0.62 $cm^3\ g^{-1}$); therefore, it gets filled faster, the favorable quadrupole interactions increase as the free space decreases, and consequently the Q_{st} curve moves upward; in fact, the CO_2 uptake by C-PAN-2×@silica(7:3)−HF−CO_2 (6.82 mmol g^{-1}) is well above what is needed for monolayer coverage of its micropores (3.6 mmol g^{-1}) and close to what is needed for filling them completely (8.6 mmol g^{-1}).

Overall, the lining of the pores is important for increased CO_2 uptake, and consistently with our previous studies, O− lining is as important as N-lining or even more so. Coverage starts with filling smaller (<1 nm) micropores and continues with monolayer coverage of small mesopores. Depending on the pore size, multilayer coverage continues until smaller mesopores (those probed with CO_2 adsorption and low-pressure N_2 sorption) are partially filled.

For practical applications, a highly CO_2-absorbing material should also be selective toward other gasses. For example, for precombustion separation, a CO_2-absorbing material should be selective against H_2 and CH_4, while for postcombustion purposes, selectivity toward N_2 is desired. The adsorption isotherms of CH_4 and H_2 at 273 K, 1 bar for both double-etched C-PUA-4.5×@silica and C-PAN-2×@silica(7:3) are shown in Figure S.14 of Appendix X in the Supporting Information. The maximum gas-uptake values are summarized in Table S.7 of Appendix X in the Supporting Information. The isotherms were fitted with a Virial-type equation that allowed calculation of the Henry's constants, K_H, for each gas and material (see Section 4). Then, selectivities were calculated as the ratios of the K_H values (see Table S.8 of Appendix X in the Supporting Information) and are compared in bar graph form in Figure 16.

The uptake of H_2 and N_2 was quite low as compared to CO_2 adsorption for carbon aerogels derived from PUA and PAN. The selectivity of C-PUA-4.5×@silica aerogels toward CO_2 versus H_2 was 624 ± 238 and 288 ± 86 for the HF−CO_2 and the CO_2−HF varieties of the material, respectively; the corresponding selectivity toward CO_2 versus N_2 was in the range of 70−80 for both varieties of the material. The significant difference in the CO_2/H_2 selectivities of C-PUA-4.5×@silica carbon aerogels from the two etching processes is attributed to the fact that the CO_2 adsorption of the HF−CO_2 variety was 50% higher than that of the CO_2−HF material (9 vs 6 mmol g^{-1}, respectively), while the H_2 adsorption was similarly low (0.06−0.08 mmol g^{-1}) for all of the double-etched PUA-derived carbon aerogels. The selectivities of the C-PAN-2×@silica-(7:3) samples toward CO_2 versus H_2 were

Beyond initial interaction with the surface walls, it is noted from Figure 15 that in the cases of C-PUA-4.5×@silica−HF−CO_2 and C-PAN-2×@silica(7:3)−CO_2−HF, the isosteric heats, Q_{st}, remained about flat until about a monolayer coverage (~6 mmol g^{-1}), and afterward they curved downwards—meaning that pore filling starts becoming less favorable. Incidentally, those are also the samples with the highest CO_2 uptake among all of the PUA- and PAN-derived carbons, respectively (Table 4). On the other hand, at first, the Q_{st} values of the other two samples, C-PUA-4.5×@silica−CO_2−HF and C-PAN-2×@silica(7:3)−HF−CO_2, trended upwards as the CO_2 uptake increased, but again they both turned downwards as pore filling progressed. Interestingly, the former two samples, whose Q_{st} plots remained substantially flat, happened to have O-rich surfaces, while the latter two samples, whose Q_{st} plots curved initially upwards, were N-rich: by XPS, the O:N atomic ratios of the HF−CO_2 etched C-PUA and C-PAN were 1.85 and 0.43, respectively, while the O:N ratio of CO_2−HF etched C-PUA and C-PAN were 0.69 and 1.02, respectively (see Table S.2 in Appendix V of the Supporting Information).

A CO_2 uptake model consistent with all data suggests that in the case of double-etched aerogels with O-rich surfaces, i.e., C-PUA-4.5×@silica−HF−CO_2 and C-PAN-2×@silica(7:3)−CO_2−HF, CO_2 is mostly adsorbed via an energy-neutral reaction with surface $-O^-$ according to eq 1 and continues beyond monolayer coverage according

$$-O^- + CO_2 \rightarrow \text{surface} - O{-}CO{-}O^- \quad (1)$$

to also energy-neutral eq 2.

$$\text{surface} - O{-}CO{-}O^- \xrightarrow{CO_2} \text{surface} - O{-}CO{-}O{-}CO{-}O^- \xrightarrow{CO_2} \text{etc.} \quad (2)$$

https://doi.org/10.1021/acs.chemmater.1c04170
Chem. Mater. 2022, 34, 4828−4847

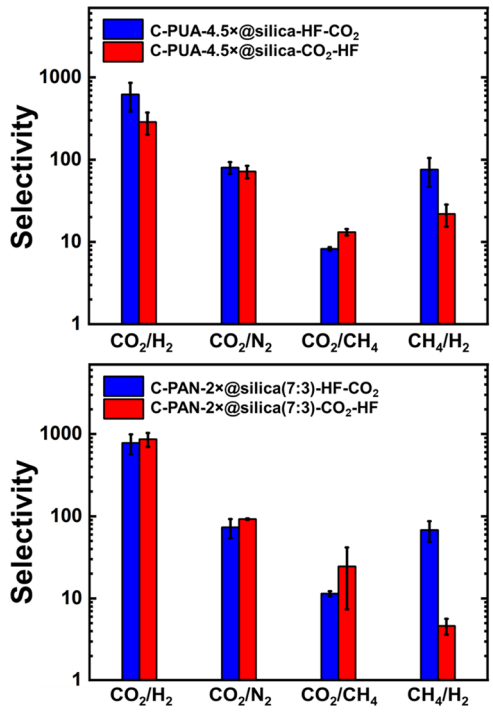

Figure 16. Relative selectivities at 273 K for the gases shown of double-etched carbon aerogels derived from PUA@silica (top) and from PAN@silica (bottom). (Selectivities were calculated as the ratios of the corresponding Henry's constants obtained by Virial fitting of the isotherms at 273 K of Figure S.14 of Appendix X in the Supporting Information).

in the range of 780−863, while CO_2/N_2 selectivities were in the range of 73−92 for materials from both etching processes. On the other hand, the adsorption of CH_4 was high compared to N_2 and H_2 (up to 2.6 mmol g^{-1}—see Table S.7 of Appendix X in the Supporting Information), which has been attributed to the high polarizability of CH_4.[56,57] As a result, selectivities of CO_2 toward methane for both PUA- and PAN-derived carbon aerogels, by both etching processes, were low, typically less than 25.

Overall, all PUA- and PAN-derived carbon aerogels by the method described here showed high selectivities toward CO_2 over H_2, which is favorable for precombustion CO_2 capture. Relevant to postcombustion applications (CO_2−N_2 separation), selectivities in the range of 71−97 were at par with those from amide networks,[58] organic cages,[59] certain conjugated organic polymers,[52] and other microporous carbon aerogels derived from phenolic aerogels.[1]

3. CONCLUSIONS

Viewing sol−gel-derived silica suspensions as removable templates for the accumulation of carbonizable polymers, we have demonstrated an alternative synthetic route to highly porous carbon aerogel monoliths from compressed polymer-cross-linked xerogel powders. The new process is energy efficient due to bypassing supercritical fluid drying or freeze-drying, time efficient due to faster solvent exchanges within the grains of wet-gel particles, and material efficient due to the reduced number of solvent exchanges required for xerogelling versus aerogelling. Post carbonization etching processes control BET/micropore surface areas as well as micro- and mesoporosities in the final carbon aerogels. The microporosity of those carbons can be utilized for high and selective CO_2 adsorption at par with the best CO_2 adsorbers considered in the literature. The method of preparing monolithic carbon aerogels from xerogel powders is generalizable and can be applied to other metal-oxide aerogels besides silica. For example, if silica is replaced with sol−gel-derived iron or cobalt oxide networks, a similar process to the one described herewith may yield graphitic aerogels at temperatures that are considered low for graphitization (e.g., ≤1500 °C).[60]

4. EXPERIMENTAL SECTION

4.1. Materials. All reagents and solvents were used as received unless noted otherwise. Ammonium hydroxide (NH_4OH, ACS reagent), 3-aminopropyltriethoxysilane (APTES), sodium hydroxide pellets (NaOH), anhydrous sodium sulfate (Na_2SO_4, ACS certified), and hydrofluoric acid (HF, 48-51% solution in water, ACS reagent) were purchased from Fisher Scientific. Tetramethylorthosilicate (TMOS), 4,4′-azobis(4-cyanopentanoic acid) (ABCVA, ≥98% *-trans*), anhydrous tetrahydrofuran (THF), and acrylonitrile (≥99%, containing 35−45 ppm monomethyl ether hydroquinone (MEHQ) as inhibitor) were purchased from the Sigma−Aldrich Chemical Company. Acrylonitrile was extracted three times with 3.0 M aqueous sodium hydroxide solution to remove the inhibitor and dried using sodium sulfate. The inhibitor-free acrylonitrile was stored in a refrigerator at 0 °C and used within a month. HPLC grade solvents including hexane, methanol (CH_3OH), ethyl acetate (EtOAc), and toluene were purchased from Fisher Scientific. Technical grade acetone was purchased from Univar (St. Louis, MO). Tris(4-isocyanatophenyl)methane (TIPM) was generously donated by Covestro LLC (Pittsburg, PA) as a 27% w/w solution in dry EtOAc under the trade name Desmodur RE (early stages of the project) and later was purchased from Shanghai Ruizheng Chemical Technology Co. (Shanghai, China) as a 27% w/w solution in dry EtOAc.[61] Ultra-high-purity Ar (grade 5), N_2 (grade 4.8), O_2 (grade), and Ar (99.99999%) gases were purchased from AirGas (Rolla, MO).

4.1.1. Preparation of APTES@Silica Powder (Refer to Scheme 2A,B). In a typical process, hexane (43 mL, 3× the volume of the intended sol) was added under flowing dry (with a drying tube) Ar (99.99999%) to a three-neck round-bottom flask equipped with a mechanical stirrer and a drying tube. To that flask, solution A consisting of 4.5 mL of CH_3OH and 3.85 mL (0.026 mol) of TMOS and solution B consisting of 4.5 mL of CH_3OH, 1.5 mL (0.083 mol) of water and 40 μL of NH_4OH were added successively at room temperature under vigorous stirring (770−950 rpm). As soon as the mixture developed fine particles and turned white (approximately 20 min), 1.28 mL (0.0065 mol) of APTES (approximately 1/3× the volume of TMOS) was added to the flask, and the reaction mixture was stirred at the same rate for 24 h at room temperature. The resulting APTES@silica suspension was transferred to centrifuge tubes (50 mL, Fisher Scientific), and the solvent was exchanged twice with ethyl acetate and once with water-saturated ethyl acetate ($EtOAc/H_2O$). After standing for 15 h in $EtOAc/H_2O$, the APTES@silica suspension was either processed to PUA@silica powder (see the next section) or dried under vacuum at 50 °C for further characterization. All washes and solvent exchanges were carried out with centrifugation for 15−20 min at 2450 rpm. Each time, the supernatant solvent was removed and the volume of the new solvent that was brought in was 2× the volume of the compacted slurry (paste) at the bottom of the centrifuge tubes. Before every new centrifugation step, the compacted slurry was resuspended with vigorous agitation with Vortex-Genie (Model no. K-550-G, Scientific Industries) and a glass rod.

4.1.2. Preparation of PUA@silica Powder (Refer to Scheme 2B). In a typical procedure, the TIPM solution as received (4× the volume of the centrifuged paste) was added to the centrifuge tubes (50 mL, Fisher Scientific, Cat. no. 06-443-18) containing the APTES@silica slurry from the last $EtOAc/H_2O$ wash; the tubes were sealed tightly with their caps, and the suspension was heated in an oven at 65 °C for 72 h. For different formulations of PUA@silica powders, different

https://doi.org/10.1021/acs.chemmater.1c04170
Chem. Mater. 2022, 34, 4828−4847

amounts of TIPM solution 4.5×, 3×, and 1.5× mol (6×, 4×, and 2× v/v relative to 1× v/v of APTES@silica paste) were used for cross-linking relative to 1× mol of APTES@silica. The mixture was swirled slowly every 10−12 h to redistribute the settled powder and increase the diffusion rate. At the end of the 3 day period, the tubes were allowed to cool to room temperature, and they were centrifuged for 15−20 min followed successively by three ethyl acetate washes. The wash solvent was always removed by centrifugation. Again, for all washes, the volume of the solvent added was twice the volume of the paste at the bottom of the tubes. After removing the solvent from the last ethyl acetate wash, the contents of the tubes were transferred with the aid of small portions of ethyl acetate and were combined in a round-bottom flask. Ethyl acetate was removed, and the product was dried under reduced pressure (water aspirator connected via a drying tube) at 50 °C into a dry, freely flowing PUA@silica powder.

4.1.3. Preparation of Initiator@Silica Powder (Refer to Scheme 2C). Hexane (43 mL, 3× the volume of the intended sol) was added under flowing dry (with a drying tube) Ar (99.99999%) to a three-neck round-bottom flask equipped with a mechanical stirrer and a drying tube. To that flask, solution A consisting of 4.5 mL of CH_3OH and 3.85 mL (0.0260 mol) of TMOS and solution B consisting of 4.5 mL of CH_3OH, 1.5 mL (0.0830 mol) of water, and 40 μL of NH_4OH were added successively at room temperature under vigorous stirring (770−950 rpm). As soon as the mixture developed fine particles and turned white (approximately 20 min), a third solution consisting of 0.67 mL (0.0028 mol) of APTES (TMOS/APTES = 9:1 mol/mol) and 0.4049 g (0.0014 mol) of ABCVA (APTES/ABCVA = 2:1 mol/mol) dissolved in 8.70 mL of anhydrous THF at 0 °C in an amber-glass Erlenmeyer flask was added to the flask. The reaction mixture was stirred at the same rate for 24 h at room temperature. The resulting initiator@silica suspension was transferred to centrifuge tubes, and the solvent was exchanged once with methanol and thrice with toluene. After this solvent exchange, the initiator@silica suspension was either processed to yield PAN@silica powder (see the next section) or was washed three times with acetone and dried under vacuum at 50 °C for further characterization. All washes and solvent exchanges were carried out with centrifugation for 15−20 min at 2450 rpm. Each time, the supernatant solvent was removed, and the volume of the new solvent that was brought in was 2× the volume of the compacted slurry (paste) at the bottom of the centrifuge tubes. Before every new centrifugation step, the compacted slurry was resuspended with vigorous agitation using Vortex-Genie (Model no. K-550-G, Scientific Industries) and a glass rod.

4.1.4. Preparation of PAN@Silica Powder (Refer to Scheme 2C). In a typical procedure, 13.5 mL of inhibitor-free acrylonitrile in 5 mL of toluene (acrylonitrile/toluene = 2.7:1 by v/v) was added in a round-bottom flask containing the above-obtained initiator@silica slurry from the toluene wash. The mixture was heated at 55 °C and stirred using a magnetic stirrer at 400 rpm. At the end of the 24 h period, the mixture was allowed to cool to room temperature and then the slurry was centrifuged for 15−20 min followed successively by three toluene washes and three acetone washes. Always, the wash solvent was removed by centrifugation. Again, for all washes, the volume of the solvent added was twice the volume of the paste at the bottom of the tubes. After removing the solvent from the last acetone wash, the contents of the tubes were transferred with the aid of small portions of acetone and were combined in a round-bottom flask. Acetone was removed and the product was dried under reduced pressure (water aspirator connected via a drying tube) at 50 °C into a dry, freely flowing PAN@silica powder.

4.1.5. Preparation, Carbonization, and Postcarbonization Etching of PUA@silica and PAN@silica Compacts (Refer to Schemes 2 and 3). Dry PUA@silica and PAN@silica powders were compressed into various cylindrical monolithic objects using a stainless-steel die and a hydraulic press operated at 10,000 psi. The placement of the powders in the die was carried out in small portions under continuous tapping.

Compressed PUA@silica compacts were converted to carbonized C-PUA@silica compacts pyrolytically at 800 °C for 5 h under flowing ultra-high-purity Ar using a programmable MTI GSL1600X-80 tube furnace (outer and inner tubes both of 99.8% pure alumina; outer tube: 1022 mm × 82 mm × 70 mm; inner tube: 610 mm × 61.45 mm × 53.55 mm; heating zone at set temperature: 457 mm). The gas flow was always set at 325 mL min^{-1}.

Compressed PAN@silica compacts were first aromatized to A-PAN@silica compacts pyrolytically at 300 °C for 24 h under flowing O_2, and then these A-PAN@silica compacts were converted to C-PAN@silica compacts pyrolytically at 800 °C for 5 h under flowing ultra-high-purity Ar.

Carbonized C-PUA@silica and C-PAN@silica compacts were subjected further to two etching processes. Hydrofluoric acid (HF, 48-51% w/w in water) treatment of carbonized C-PUA@silica and C-PAN@silica compacts was carried out in high-density polyethylene (HDPE) vials (20 mL, Cat. no. 03-337-23, Fisher Scientific) capped with rubber septa (Cat. no. CG-3024-03, ChemGlass Life Sciences) under reduced pressure (using a water aspirator) until no more bubbles were observed coming out from the carbonized compacts. Subsequently, these compacts were washed three times with distilled water and three times with acetone in the same HDPE vials, under reduced pressure, for 15 min each time. Finally, washed compacts were dried in a vacuum oven at 80 °C for 24 h. CO_2 etching was carried out in a tube furnace at 1000 °C for 3 h under flowing CO_2, before or after HF treatment.

4.2. Methods. *4.2.1. Physical Characterization.* Bulk densities (ρ_b) were calculated from weight and physical dimensions of the samples. Skeletal densities (ρ_s) were measured using helium pycnometry on a Micromeritics AccuPyc II 1340 instrument. Samples for skeletal density measurements were outgassed for 24 h at 80 °C under vacuum before analysis. Percent porosities (Π) were determined from the ρ_b and ρ_s values via $\Pi = 100 \times [(\rho_s - \rho_b)/\rho_s]$.

4.2.2. Chemical Characterization. Different methods were applied at different stages of processing as follows.

Liquid ^{13}C NMR spectra were recorded with 400 MHz Varian Unity Inova NMR instrument (100 MHz carbon frequency). The cross-linked polymer was identified as polyacrylonitrile with solid-state CPMAS ^{13}C NMR on a Bruker Avance III 400 MHz spectrometer with a carbon frequency 100 MHz, using 7 mm Bruker MAS probe at a magic angle spinning rate of 5 kHz with broadband proton suppression and CP total suppression of spinning side bands (TOSS) pulse sequence. The TOSS pulse sequence was applied using a series of four properly timed 180° pulses on the carbon channel at different points of a cycle before the acquisition of the FID, after an initial excitation with a 90° pulse on the proton channel. The 90° excitation pulse on the proton and the 180° excitation pulse on carbon were set to 4.2 and 10 μs, respectively. The cross-polarization contact time and the relaxation delay were set at 3000 μs and 5 s, respectively. The number of scans was set at 2048. Spectra were referenced externally to glycine (carbonyl carbon at 176.03 ppm). Chemical shifts were reported versus tetramethylsilane (TMS, 0 ppm). Solid-state ^{29}Si NMR spectra were also obtained on the same Bruker Avance III 400 MHz spectrometer with a 59.624 MHz silicon frequency using again a 7 mm Bruker MAS probe and magic angle spinning at 5 kHz, using cross-polarization pulse sequence. The cross-polarization contact time and the relaxation delay were set at 3000 μs and 5 s, respectively. The number of scans was set at 16384. ^{29}Si NMR spectra were referenced externally to neat TMS (0 ppm).

X-ray photoelectron spectroscopic analysis (XPS) was carried out with a Thermo Fischer Scientific Nexsa X-ray Photoelectron Spectrometer System. Samples were mixed and ground together with Au powder (5% w/w) as an internal reference. Deconvolution of the spectra was performed with Gaussian function fitting using the OriginPro 9.7 software package.

4.2.3. Thermal Characterization. Thermogravimetric analysis (TGA) was conducted under air at 1000 °C with Fischer Scientific Isotemp muffle furnace using a heating rate of 10 °C min^{-1}. TGA was also conducted under O_2 with a TA instrument Model TGA Q50 analyzer, using a heating rate of 5 °C min^{-1}.

Modulated differential scanning calorimetry (MDSC) was conducted under N_2 from -30 to 350 °C, with a heating rate of 5 °C

https://doi.org/10.1021/acs.chemmater.1c04170
Chem. Mater. 2022, 34, 4828−4847

min^{-1} using a TA Instruments Differential Scanning Calorimeter Model Q2000.

4.2.4. Structural Characterization. Scanning electron microscopy (SEM) and energy-dispersive X-ray spectroscopy (SEM-EDX) were conducted with Au/Pd (60/40)-coated samples on a Hitachi Model S-4700 field-emission microscope. Samples were placed on the stub using C-dot. Thin sticky copper strips were cut and placed on the edges and top of the sample, leaving space for the analysis.

4.2.5. Pore Structure Analysis. The pore structure was probed with N_2-sorption porosimetry at 77 K using either a Micromeritics ASAP 2020 or a TriStar II 3020 surface area and porosimetry analyzer. Before porosimetry, samples were outgassed for 24 h under vacuum at 120 °C. Data were reduced to standard conditions of temperature and pressure (STP). Total surface areas were determined via the Brunauer–Emmett–Teller (BET) method from the N_2-sorption isotherms. Micropore analysis was conducted with low-pressure N_2-sorption at 77 K using a Micromeritics ASAP 2020 instrument equipped with a low-pressure transducer or with CO_2 adsorption up to 760 Torr (relative pressure P/P_0 = 0.03) at 273 K using the Micromeritics TriStar II 3020 system mentioned above. Micropore surface areas were calculated via t-plot analysis of the isotherms using the Harkins and Jura Model. Pore size distributions were determined with the Barret–Joyne–Halenda (BJH) equation applied to the desorption branch of the N_2-sorption isotherms.

4.2.6. Isosteric Heats of CO_2 Adsorption (Q_{st}). Q_{st} values were calculated using the Virial fitting method. For this, the CO_2 adsorption isotherms at 273 and 298 K were fitted simultaneously with a Virial-type eq 3 using the OriginPro 2020 9.7.0 software package.

$$\ln P = \ln N + \frac{1}{T}\sum_{i=0}^{m} a_i N^i + \sum_{i=0}^{n} b_i N^i \tag{3}$$

where P is pressure in Torr, N is the adsorbed amount in mmol g^{-1}, T is the absolute temperature, a_i and b_i are the Virial coefficients, and m and n are the number of coefficients (or polynomial terms) needed to fit the isotherms adequately. Using the least-squares method, the values of m and n were gradually increased until the sum of the squared deviations of the experimental points from the fitted isotherm was minimized. All data were fitted well with m = 3 and n = 1 (see Table S.5 in Appendix IX of the Supporting Information). The values of a_o to a_m were introduced into eq 4, and the isosteric heats of adsorption (Q_{st}) were calculated as a function of the surface coverage (N).

$$Q_{st} = -R\sum_{i=0}^{m} a_i N^i \tag{4}$$

where R is the gas constant (8.314 J mol^{-1} K^{-1}) and Q_{st} is given in kJ mol^{-1}. The common term in eq 4 for all N, Q_0, corresponds to i = 0 and is given by eq 5.

$$Q_0 = -Ra_0 \tag{5}$$

Q_0 is the heat of adsorption as coverage goes to zero and is a sensitive evaluator of the affinity of the adsorbate for the surface. Q_0 values are summarized in Table S.6 of Appendix IX in the Supporting Information.

4.2.7. Relative Adsorption Selectivities. Relative adsorption studies for CO_2, CH_4, N_2, and H_2 were done on a Micromeritics TriStar II 3020 surface area and porosimetry analyzer at 273 K up to 1 bar. Adsorption selectivities for one gas versus another were calculated as the ratios of the respective Henry's constants, K_H. The latter were calculated via another type of a Virial model, whereas the single-component adsorption isotherms for each gas at 273 K were fitted according to eq 6.

$$\ln N = \ln P + K_1 + K_2 N + K_3 N^2 + \ldots = \ln P + \sum_{i=1}^{m} K_i N^{i-1} \tag{6}$$

Fitting was carried out using the least-squares method by varying the number of terms, until a suitable number of terms, m, described the isotherms adequately. Coefficients K_1, K_2, ..., K_m are characteristic constants for a given gas–solid system and temperature. The Henry's constant for each gas, K_H, is the limiting value of N/P as $P \to 0$ and is given by eq 7.[62]

$$K_H = \lim_{P\to 0}\left(\frac{N}{P}\right) \cong e^{K_1} \tag{7}$$

To calculate standard deviations, all isotherms obtained experimentally for each component were fitted individually. The K_H values from all isotherms were averaged, and the average values were used to calculate selectivities by taking the ratios. Standard deviations for the ratios were calculated using rules for propagation of error.

■ ASSOCIATED CONTENT

Supporting Information

The Supporting Information is available free of charge at https://pubs.acs.org/doi/10.1021/acs.chemmater.1c04170.

Appendix I (Thermogravimetric analysis (TGA) data); Appendix II (CPMAS ^{13}C NMR spectra of PAN and of A-PAN-n×@silica(x:y) compacts along the aromatization process); Appendix III (Solid-state ^{29}Si and ^{13}C CPMAS NMR spectra of all as-prepared PUA@silica and PAN@silica compacts); Appendix IV (EDS data of carbonized PUA@silica and PAN@silica samples before and after HF treatment); Appendix V (XPS data of carbonized samples before and after etching with HF and CO_2 in either sequence); Appendix VI (Tables of materials characterization data); Appendix VII (References cited in Figure 13); Appendix VIII (Micropore size distribution by the CO_2/DFT method); Appendix IX (Virial fitting of CO_2 isotherms at 273 and 298 K); and Appendix X (Adsorption selectivities of various gasses at 273 K) (PDF)

■ AUTHOR INFORMATION

Corresponding Author

Chariklia Sotiriou-Leventis − *Department of Chemistry, Missouri University of Science and Technology, Rolla, Missouri 65409, United States;* orcid.org/0000-0003-3283-8257; Phone: 573-341-4353; Email: cslevent@mst.edu

Authors

Rushi U. Soni − *Department of Chemistry, Missouri University of Science and Technology, Rolla, Missouri 65409, United States*

Vaibhav A. Edlabadkar − *Department of Chemistry, Missouri University of Science and Technology, Rolla, Missouri 65409, United States;* orcid.org/0000-0001-5763-7318

Daniel Greenan − *Department of Chemistry, Missouri University of Science and Technology, Rolla, Missouri 65409, United States*

Parwani M. Rewatkar − *Department of Chemistry, Missouri University of Science and Technology, Rolla, Missouri 65409, United States*

Nicholas Leventis − *Department of Chemistry, Missouri University of Science and Technology, Rolla, Missouri 65409, United States;* Present Address: Aspen Aerogels, 30 Forbes Road, Bldg. B, Northborough, Massachusetts 01532, United States

Complete contact information is available at:

https://pubs.acs.org/10.1021/acs.chemmater.1c04170

Notes

The authors declare no competing financial interest.

■ ACKNOWLEDGMENTS

The authors thank the NSF for financial support under award number CMMI-1530603 (subcontract to MS&T from Tufts University).

■ REFERENCES

(1) Majedi Far, H.; Rewatkar, P. M.; Donthula, S.; Taghvaee, T.; Saeed, A. M.; Sotiriou-Leventis, C.; Leventis, N. Exceptionally High CO_2 Adsorption at 273 K by Microporous Carbons from Phenolic Aerogels: The Role of Heteroatoms in Comparison with Carbons from Polybenzoxazine and Other Organic Aerogels. *Macromol. Chem. Phys.* **2019**, *220*, No. 1800333.

(2) Park, J.; Jung, M.; Jang, H.; Lee, K.; Attia, N. F.; Oh, H. A Facile Synthesis Tool of Nanoporous Carbon for Promising H_2, CO_2, and CH_4 Sorption Capacity and Selective Gas Separation. *J. Mater. Chem. A* **2018**, *6*, 23087−23100.

(3) Li, Z.; Xu, J.; Sun, D.; Lin, T.; Huang, F. Nanoporous Carbon Foam for Water and Air Purification. *ACS Appl. Nano Mater.* **2020**, *3*, 1564−1570.

(4) Lam, E.; Luong, J. H. T. Carbon Materials as Catalyst Supports and Catalysts in the Transformation of Biomass to Fuels and Chemicals. *ACS Catal.* **2014**, *4*, 3393−3410.

(5) Xue, Y.; Xie, J.; He, M.; Liu, M.; Xu, M.; Ni, W.; Yan, Y. M. Porous and High-Strength Graphitic Carbon/SiC Three-Dimensional Electrode for Capacitive Deionization and Fuel Cell Applications. *J. Mater. Chem. A* **2018**, *6*, 19210−19220.

(6) Far, H. M.; Donthula, S.; Taghvaee, T.; Saeed, A. M.; Garr, Z.; Sotiriou-Leventis, C.; Leventis, N. Air-Oxidation of Phenolic Resin Aerogels: Backbone Reorganization, Formation of Ring-Fused Pyrylium Cations, and the Effect on Microporous Carbons with Enhanced Surface Areas. *RSC Adv.* **2017**, *7*, 51104−51120.

(7) Mahadik-Khanolkar, S.; Donthula, S.; Sotiriou-Leventis, C.; Leventis, N. Polybenzoxazine Aerogels. 1. High-Yield Room-Temperature Acid-Catalyzed Synthesis of Robust Monoliths, Oxidative Aromatization, and Conversion to Microporous Carbons. *Chem. Mater.* **2014**, *26*, 1303−1317.

(8) Saeed, A. M.; Rewatkar, P. M.; Majedi Far, H.; Taghvaee, T.; Donthula, S.; Mandal, C.; Sotiriou-Leventis, C.; Leventis, N. Selective CO_2 Sequestration with Monolithic Bimodal Micro/Macroporous Carbon Aerogels Derived from Stepwise Pyrolytic Decomposition of Polyamide-Polyimide-Polyurea Random Copolymers. *ACS Appl. Mater. Interfaces* **2017**, *9*, 13520−13536.

(9) Sadekar, A. G.; Mahadik, S. S.; Bang, A. N.; Larimore, Z. J.; Wisner, C. A.; Bertino, M. F.; Kalkan, A. K.; Mang, J. T.; Sotiriou-Leventis, C.; Leventis, N. From "Green" Aerogels to Porous Graphite by Emulsion Gelation of Acrylonitrile. *Chem. Mater.* **2012**, *24*, 26−47.

(10) Chang, J.; Zhang, Q.; Lin, Y.; Zhou, C.; Yang, W.; Yan, L.; Wu, G. Carbon Nanotubes Grown on Graphite Films as Effective Interface Enhancement for an Aluminum Matrix Laminated Composite in Thermal Management Applications. *ACS Appl. Mater. Interfaces* **2018**, *10*, 38350−38358.

(11) Zou, J.; Liu, J.; Karakoti, A. S.; Kumar, A.; Joung, D.; Li, Q.; Khondaker, S. I.; Seal, S.; Zhai, L. Ultralight Multiwalled Carbon Nanotube Aerogel. *ACS Nano* **2010**, *4*, 7293−7302.

(12) Ieamviteevanich, P.; Palaporn, D.; Chanlek, N.; Poo-Arporn, Y.; Mongkolthanaruk, W.; Eichhorn, S. J.; Pinitsoontorn, S. Carbon Nanofiber Aerogel/Magnetic Core-Shell Nanoparticle Composites as Recyclable Oil Sorbents. *ACS Appl. Nano Mater.* **2020**, *3*, 3939−3950.

(13) Kuang, J.; Liu, L.; Gao, Y.; Zhou, D.; Chen, Z.; Han, B.; Zhang, Z. A Hierarchically Structured Graphene Foam and Its Potential as a Large-Scale Strain-Gauge Sensor. *Nanoscale* **2013**, *5*, 12171−12177.

(14) Wang, J.; Kaskel, S. KOH Activation of Carbon-Based Materials for Energy Storage. *J. Mater. Chem.* **2012**, *22*, 23710−23725.

(15) Tseng, R. L. Mesopore Control of High Surface Area NaOH-Activated Carbon. *J. Colloid Interface Sci* **2006**, *303*, 494−502.

(16) Chang, B.; Wang, Y.; Pei, K.; Yang, S.; Dong, X. $ZnCl_2$-Activated Porous Carbon Spheres with High Surface Area and Superior Mesoporous Structure as an Efficient Supercapacitor Electrode. *RSC Adv.* **2014**, *4*, 40546−40552.

(17) Bedia, J.; Belver, C.; Ponce, S.; Rodriguez, J.; Rodriguez, J. J. Adsorption of Antipyrine by Activated Carbons from $FeCl_3$-Activation of Tara Gum. *Chem. Eng. J.* **2018**, *333*, 58−65.

(18) Zbair, M.; Ainassaari, K.; El Assal, Z.; Ojala, S.; El Ouahedy, N.; Keiski, R. L.; Bensitel, M.; Brahmi, R. Steam Activation of Waste Biomass: Highly Microporous Carbon, Optimization of Bisphenol A, and Diuron Adsorption by Response Surface Methodology. *Environ. Sci. Pollut. Res.* **2018**, *25*, 35657−35671.

(19) Scherer, G. W. *Xerogels Encyclopedia of Materials: Science and Technology*, Buschow, K. H. J.; Cahn, R. W.; Flemings, M. C.; Ilschner, B.; Kramer, E. J.; Mahajan, S.; Veyssière, P., Eds.; Elsevier: New Jersey, 2001; pp 9797−9799.

(20) Rewatkar, P. M.; Taghvaee, T.; Saeed, A. M.; Donthula, S.; Mandal, C.; Chandrasekaran, N.; Leventis, T.; Shruthi, T. K.; Sotiriou-Leventis, C.; Leventis, N. Sturdy, Monolithic SiC and Si_3N_4 Aerogels from Compressed Polymer-Cross-Linked Silica Xerogel Powders. *Chem. Mater.* **2018**, *30*, 1635−1647.

(21) Rewatkar, P. M.; Soni, R. U.; Sotiriou-Leventis, C.; Leventis, N. A Cobalt Sunrise: Thermites Based on $LiClO_4$-Filled Co(0) Aerogels Prepared from Polymer-Cross-Linked Cobaltia Xerogel Powders. *ACS Appl. Mater. Interfaces* **2019**, *11*, 22668−22676.

(22) Leventis, N. Three-Dimensional Core-Shell Superstructures: Mechanically Strong Aerogels. *Acc. Chem. Res.* **2007**, *40*, 874−884.

(23) Leventis, N.; Elder, I. A.; Rolison, D. R.; Anderson, M. L.; Merzbacher, C. I. Durable Modification of Silica Aerogel Monoliths with Fluorescent 2,7-Diazapyrenium Moieties. Sensing Oxygen near the Speed of Open-Air Diffusion. *Chem. Mater.* **1999**, *11*, 2837−2845.

(24) Hüsing, N.; Schubert, U.; Mezei, R.; Fratzl, P.; Riegel, B.; Kiefer, W.; Kohler, D.; Mader, W. Formation and Structure of Gel Networks from $Si(OEt)_4$/ $(MeO)_3Si(CH_2)_3NR'_2$ Mixtures (NR'_2 = NH_2 or $NHCH_2CH_2NH_2$). *Chem. Mater.* **1999**, *11*, 451−457.

(25) Zha, J.; Roggendorf, H. Sol−Gel Science, the Physics and Chemistry of Sol−Gel Processing, Ed. by C. J. Brinker and G. W. Scherer, Academic Press, Boston 1990, Xiv, 908 Pp., Bound—ISBN 0-12-134970-5. *Adv. Mater.* **1991**, *3*, 522.

(26) Leventis, N.; Sotiriou-Leventis, C.; Zhang, G.; Rawashdeh, A. M. M. Nanoengineering Strong Silica Aerogels. *Nano Lett.* **2002**, *2*, 957−960.

(27) Zhang, G.; Dass, A.; Rawashdeh, A. M. M.; Thomas, J.; Counsil, J. A.; Sotiriou-Leventis, C.; Fabrizio, E. F.; Ilhan, F.; Vassilaras, P.; Scheiman, D. A.; McCorkle, L.; Palczer, A.; Johnston, J. C.; Meador, M. A.; Leventis, N. Isocyanate-Crosslinked Silica Aerogel Monoliths: Preparation and Characterization. *J. Non-Cryst. Solids* **2004**, *350*, 152−164.

(28) Leventis, N.; Sotiriou-Leventis, C.; Chandrasekaran, N.; Mulik, S.; Larimore, Z. J.; Lu, H.; Churu, G.; Mang, J. T. Multifunctional Polyurea Aerogels from Isocyanates and Water. A Structure-Property Case Study. *Chem. Mater.* **2010**, *22*, 6692−6710.

(29) Mulik, S.; Sotiriou-Leventis, C.; Churu, G.; Lu, H.; Leventis, N. Cross-Linking 3D Assemblies of Nanoparticles into Mechanically Strong Aerogels by Surface-Initiated Free-Radical Polymerization. *Chem. Mater.* **2008**, *20*, 5035−5046.

(30) Leventis, N.; Sadekar, A.; Chandrasekaran, N.; Sotiriou-Leventis, C. Click Synthesis of Monolithic Silicon Carbide Aerogels from Polyacrylonitrile-Coated 3D Silica Networks. *Chem. Mater.* **2010**, *22*, 2790−2803.

(31) Li, J.; Huang, X.; Chen, L. X-Ray Diffraction and Vibrational Spectroscopic Studies on PAN-LiTFSI Polymer Electrolytes. *J. Electrochem. Soc.* **2000**, *147*, 2653.

(32) Wang, Y.-X.; Wang, Q. Evaluation of Carbonization Tar in Making High Performance Polyacrylonitrile-Based Carbon Fibers. *J. Appl. Polym. Sci.* **2007**, *104*, 1255−1259.

(33) Usami, T.; Itoh, T.; Ohtani, H.; Tsuge, S. Structural Study of Polyacrylonitrile Fibers During Oxidativi Thermal Degradation by Pyrolysis-Gas Chromatography, Solid-State ^{13}C Nuclear Magnetic Resonance, and Fourier Transform Infrared Spectroscopy. *Macromolecules* **1990**, *23*, 2460−2465.
(34) Leventis, N.; Sotiriou-Leventis, C.; Saeed, A. M.; Donthula, S.; Majedi Far, H.; Rewatkar, P. M.; Kaiser, H.; Robertson, J. D.; Lu, H.; Churu, G. Nanoporous Polyurea from a Triisocyanate and Boric Acid: A Paradigm of a General Reaction Pathway for Isocyanates and Mineral Acids. *Chem. Mater.* **2016**, *28*, 67−78.
(35) Gross, T.; Ramm, M.; Sonntag, H.; Unger, W.; Weijers, H. M.; Adem, E. H. An XPS Analysis of Different SiO_2 Modifications Employing a C 1s as Well as an Au 4f7/2 Static Charge Reference. *Surf. Interface Anal.* **1992**, *18*, 59−64.
(36) Bertoncello, R.; Glisenti, A.; Granozzi, G.; Battaglin, G.; Caccavale, F.; Cattaruzza, E.; Mazzoldi, P. Chemical Interactions in Titanium- and Tungsten-Implanted Fused Silica. *J. Non-Cryst. Solids* **1993**, *162*, 205−216.
(37) Kim, C. M.; Jeong, H. S.; Kim, E. H. NEXAFS and XPS Characterization of Molecular Oxygen Adsorbed on Ni(100) at 80 K. *Surf. Sci.* **2000**, *459*, L457−L461.
(38) Figueiredo, J. L.; Pereira, M. F. R. The Role of Surface Chemistry in Catalysis with Carbons. *Catal. Today* **2010**, *150*, 2−7.
(39) Figueiredo, J. L.; Pereira, M. F. R.; Freitas, M. M. A.; Órfão, J. J. M. Modification of the Surface Chemistry of Activated Carbons. *Carbon* **1999**, *37*, 1379−1389.
(40) Chen, J.; Mao, Z.; Zhang, L.; Tang, Y.; Wang, D.; Bie, L.; Fahlman, B. D. Direct Production of Nitrogen-Doped Porous Carbon from Urea via Magnesiothermic Reduction. *Carbon* **2018**, *130*, 41−47.
(41) Moon, I. K.; Lee, J.; Lee, H. Highly Qualified Reduced Graphene Oxides: The Best Chemical Reduction. *Chem. Commun.* **2011**, *47*, 9681−9683.
(42) Inagaki, M.; Toyoda, M.; Soneda, Y.; Morishita, T. Nitrogen-Doped Carbon Materials. *Carbon* **2018**, *132*, 104−140.
(43) Riedo, E.; Comin, F.; Chevrier, J.; Schmithusen, F.; Decossas, S.; Sancrotti, M. Structural Properties and Surface Morphology of Laser-Deposited Amorphous Carbon and Carbon Nitride Films. *Surf. Coat. Technol.* **2000**, *125*, 124−128.
(44) Scharf, T. W.; Ott, R. D.; Yang, D.; Barnard, J. A. Structural and Tribological Characterization of Protective Amorphous Diamond-like Carbon and Amorphous CN_x Overcoats for next Generation Hard Disks. *J. Appl. Phys.* **1999**, *85*, 3142−3154.
(45) Yan, X.; Xu, T.; Chen, G.; Xu, S.; Yang, S. Field-Emission Properties of Diamond-like-Carbon and Nitrogen-Doped Diamond-like-Carbon Films Prepared by Electrochemical Deposition. *Appl. Phys. A: Mater. Sci. Process.* **2005**, *81*, 41−46.
(46) Wickramaratne, N. P.; Jaroniec, M. Importance of Small Micropores in CO_2 Capture by Phenolic Resin-Based Activated Carbon Spheres. *J. Mater. Chem. A* **2013**, *1*, 112−116.
(47) Adeniran, B.; Mokaya, R. Low Temperature Synthesized Carbon Nanotube Superstructures with Superior CO_2 and Hydrogen Storage Capacity. *J. Mater. Chem. A* **2015**, *3*, 5148−5161.
(48) Webb, P. A.; Orr, C. *Analytical Methods in Fine Particle Technology*, Micromeritics Instrument Corporation: Norcross, GA, 1997; pp 61−66.
(49) Cazorla-Amorós, D.; Alcaniz-Monge, J.; Linares-Solano, A. Characterization of Activated Carbon Fibers by CO_2 Adsorption. *Langmuir* **1996**, *12*, 2820−2824.
(50) Cazorla-Amorós, D.; Alcañiz-Monge, J.; De La Casa-Lillo, M. A.; Linares-Solano, A. CO_2 as an Adsorptive to Characterize Carbon Molecular Sieves and Activated Carbons. *Langmuir* **1998**, *14*, 4589−4596.
(51) Smit, B.; Reimer, J. R.; Oldenburg, C. M.; Bourg, I. C. *Introduction to Carbon Capture and Sequestration: The Berkeley Lectures on Energy*, Imperial College Press: London, 2014; Vol. *1*, pp 281−354.
(52) Patel, H. A.; Je, S. H.; Park, J.; Jung, Y.; Coskun, A.; Yavuz, C. T. Directing the Structural Features of N_2-Phobic Nanoporous Covalent Organic Polymers for CO_2 Capture and Separation. *Chem. - Eur. J.* **2014**, *20*, 772−780.
(53) Germain, J.; Fréchet, J. M. J.; Svec, F. Nanoporous Polymers for Hydrogen Storage. *Small* **2009**, *5*, 1098−1111.
(54) Xydias, P.; Spanopoulos, I.; Klontzas, E.; Froudakis, G. E.; Trikalitis, P. N. Drastic Enhancement of the CO_2 Adsorption Properties in Sulfone-Functionalized Zr- and Hf-UiO-67 MOFs with Hierarchical Mesopores. *Inorg. Chem.* **2014**, *53*, 679−681.
(55) Yang, X.; Yu, M.; Zhao, Y.; Zhang, C.; Wang, X.; Jiang, J. X. Hypercrosslinked Microporous Polymers Based on Carbazole for Gas Storage and Separation. *RSC Adv.* **2014**, *4*, 61051−61055.
(56) Bag, S.; Kanatzidis, M. G. Chalcogels: Porous Metal-Chalcogenide Networks from Main-Group Metal Ions. Effect of Surface Polarizability on Selectivity in Gas Separation. *J. Am. Chem. Soc.* **2010**, *132*, 14951−14959.
(57) Rallapalli, P.; Prasanth, K. P.; Patil, D.; Somani, R. S.; Jasra, R. V.; Bajaj, H. C. Sorption Studies of CO_2, CH_4, N_2, CO, O_2 and Ar on Nanoporous Aluminum Terephthalate [MIL-53(Al)]. *J. Porous Mater.* **2011**, *18*, 205−210.
(58) Jin, Y.; Voss, B. A.; Noble, R. D.; Zhang, W. A Shape-Persistent Organic Molecular Cage with High Selectivity for the Adsorption of CO_2 over N_2. *Angew. Chem., Int. Ed.* **2010**, *49*, 6348−6351.
(59) Zulfiqar, S.; Mantione, D.; El Tall, O.; Sarwar, M. I.; Ruipérez, F.; Rothenberger, A.; Mecerreyes, D. Nanoporous Amide Networks Based on Tetraphenyladamantane for Selective CO_2 Capture. *J. Mater. Chem. A* **2016**, *4*, 8190−8197.
(60) Soni, R. U.; Edlabadkar, V. A.; Rewatkar, P. M.; ud Doulah, A. B. M. S.; Leventis, N.; Sotiriou-Leventis, C. Low-temperature Catalytic Synthesis of Graphite Aerogels from Polyacrylonitrile-crosslinked Iron Oxide and Cobalt Oxide Xerogel Powders. *Carbon* **2022**, *193*, 107−127.
(61) https://www.alibaba.com/product-detail/Desmodur-Re-China-Factory-Offer-Best_1600316871996.html?spm=a2700.galleryofferlist.normal_offer.d_title.1186628e03OPci&s=p (March 25, 2022).
(62) Sing, K. S. W.; Rouquerol, J. Classical Interpretation of Physisorption Isotherms at the Gas − Solid Interface. In *Adsorption by Powders and Porous Solids*, 2nd ed.; Rouquerol, F.; Rouquerol, J.; Sing, K. S. W.; Liewwllyn, P.; Maurin, G., Eds.; Principles, Methodology and Applications; Academic Press: Oxford, 2014; pp 159−189.

https://doi.org/10.1021/acs.chemmater.1c04170
Chem. Mater. 2022, 34, 4828−4847